

Article

Monitoring Trends of CO, NO₂, SO₂, and O₃ Pollutants Using Time-Series Sentinel-5 Images Based on Google Earth Engine

Mohammad Kazemi Garajeh ¹, Giovanni Laneve ^{2,*}, Hamid Rezaei ³, Mostafa Sadeghnejad ⁴,
Neda Mohamadzadeh ⁴ and Behnam Salmani ⁵

¹ Department of Civil, Constructional and Environmental Engineering, Sapienza University of Rome, 00185 Rome, Italy

² School of Aerospace Engineering (SIA), Sapienza University of Rome, Via Salaria 851-881, 00138 Rome, Italy

³ Department of Civil and Environmental Engineering, Florida International University, Miami, FL 33199, USA

⁴ Department of Geography and Geospatial Sciences, Kansas State University, 920 N17th Street, Manhattan, KS 66506, USA

⁵ Department of Remote Sensing and GIS, University of Tabriz, Tabriz 5166616471, Iran

* Correspondence: giovanni.laneve@uniroma1.it

Abstract: Air pollution (AP) is a significant risk factor for public health, and its impact is becoming increasingly concerning in developing countries where it is causing a growing number of health issues. It is therefore essential to map and monitor AP sources in order to facilitate local action against them. This study aims at assessing the suitability of Sentinel-5 AP products based on Google Earth Engine (GEE) to monitor air pollutants, including CO, NO₂, SO₂, and O₃ in Arak city, Iran from 2018 to 2019. Our process involved feeding satellite images to a cloud-free GEE platform that identified pollutant-affected areas monthly, seasonally, and annually. By coding in the JavaScript language in the GEE, four pollution parameters of Sentinel-5 satellite images were obtained. Following that, images with clouds were filtered by defining cloud filters, and average maps were extracted by defining average filters for both years. The employed model, which solely used Sentinel-5 AP products, was tested and assessed using ground data collected from the Environmental Organization of Central Province. Our findings revealed that annual CO, NO₂, SO₂, and O₃ were estimated with RMSE of 0.13, 2.58, 4.62, and 2.36, respectively, for the year 2018. The annual CO, NO₂, SO₂, and O₃ for the year 2019 were also calculated with RMSE of 0.17, 2.41, 4.31, and 4.6, respectively. The results demonstrated that seasonal AP was estimated with RMSE of 0.09, 5.39, 0.70, and 7.81 for CO, NO₂, SO₂, and O₃, respectively, for the year 2018. Seasonal AP was also estimated with RMSE of 0.12, 4.99, 1.33, and 1.27 for CO, NO₂, SO₂, and O₃, respectively, for the year 2019. The results of this study revealed that Sentinel-5 data combined with automated-based approaches, such as GEE, can perform better than traditional approaches (e.g., pollution measuring stations) for AP mapping and monitoring since they are capable of providing spatially distributed data that is sufficiently accurate.

Keywords: air pollution; remote sensing; Google Earth Engine (GEE); Sentinel-5; Arak city



Citation: Kazemi Garajeh, M.; Laneve, G.; Rezaei, H.; Sadeghnejad, M.; Mohamadzadeh, N.; Salmani, B. Monitoring Trends of CO, NO₂, SO₂, and O₃ Pollutants Using Time-Series Sentinel-5 Images Based on Google Earth Engine. *Pollutants* **2023**, *3*, 255–279. <https://doi.org/10.3390/pollutants3020019>

Academic Editor: Farshad Amiraslani

Received: 1 March 2023

Revised: 21 April 2023

Accepted: 25 April 2023

Published: 22 May 2023



Copyright: © 2023 by the authors. Licensee MDPI, Basel, Switzerland. This article is an open access article distributed under the terms and conditions of the Creative Commons Attribution (CC BY) license (<https://creativecommons.org/licenses/by/4.0/>).

1. Introduction

In today's world, air pollution (AP) is one of the most destructive challenges to the quality of life, especially in developing countries [1]. With the rapid expansion of urbanization and the development of cities, along with rapid population growth, industrialization, and the indiscriminate use of fossil fuels, pollution has increased and exceeded the capacity of the environment to tolerate it [2,3]. As a result, citizens are more likely to suffer from respiratory diseases and suffer from worsened heart and lung conditions. Furthermore, environmental damage, including damage caused by air pollution, costs billions of dollars every year in financial credits, human labor, and other resources [4–6].

In recent years, AP has become a leading cause of death in both developing and developed countries [7]. In this regard, the amount of air pollutants in many cities in

Iran has reached dangerous levels, including in Tehran, Mashhad, Isfahan, Tabriz, Shiraz, Karaj, Arak and Ahvaz [8–11]. Among the various sectors that pollute the air in Iran, the transportation and industry sectors both generate the most pollution; the transportation sector alone emits 63.3% of the total nitrogen oxide emissions, 29.3% of sulfur dioxide emissions, 27.5% of carbon dioxide emissions, 24.8% of sulfur trioxide emissions, 98.6% of carbon monoxide emissions, 96.3% of carbon hydride emissions, and 79.2% of suspended particles. Tehran's air pollution, for instance, is linked to 70% of deaths, according to studies by the Environmental Organization [12,13].

Pollution measuring stations are one of the most accurate methods of measuring pollution. However, measurements are limited to the area around the stations [14,15]. Because of their high installation and maintenance costs, this solution is not widely used in managing and monitoring pollution. By relying solely on ground values, complex air pollution models that include things such as the source, movement path, and chemical characteristics of different types of pollution also have problems [16]. Measurements from pollution stations provide accurate and temporally discrete AP information; however, these measurements are often affected by significant errors associated with them and often result in unrepresentative spatial patterns [17]. Additionally, as temporal resolution and temperature extremes increase, the complexity of AP patterns increases. It is, thus, necessary to use remote sensing methods that have acceptable temporal and spatial resolution in order to overcome these problems [18,19]. In this regard, Sentinel satellites have provided key information in various fields of global monitoring for environmental management programs, understanding and dealing with the effects of climate change, water resources management, hydrology, monitoring the expansion and change of megacities, forests, and agricultural areas, and monitoring plant productivity and health [20–22]. Sentinel-5 is the first mission of the Copernicus air pollution control program. Sentinel-5 can be used for identifying ozone, methane, formaldehyde, aerosol, carbon monoxide, NO₂, and SO₂ gases [23]. Satellite images from Sentinel-5 can be effective in investigating the spatial distribution of pollutants due to their large and global observations of the Earth's surface. As part of Sentinel-5, the TROPOMI (TROPOspheric Monitoring Instrument) sensor provides daily data on air pollution [24]. There is a wide range of pollutants that can be monitored and imaged using the TROPOMI sensor. There are three different ways to obtain images of these pollutants: real-time images, offline images, and reprocessing images. Almost instantaneous data is available within three hours of data acquisition, and offline data is available several days after imaging [25].

With improvements in the variety and resolution of remote sensing data, various semi-automated and automated methods have been developed, such as Google Earth Engine [26]. GEE is an online computing platform that processes satellite images, spatial data, and geographical data at the petabyte scale [27]. This web-based system provides access to satellite data processing software and algorithms [28]. The GEE makes it relatively easy to access satellite data and other information, cloud computing, and big data processing algorithms [29,30]. The GEE system provides researchers with easy and high-speed access to over thirty years' worth of free and public data archives, including old images and scientific datasets for large-scale sensing applications [31]. In this way, many limitations related to downloading, storing and processing data are easily overcome [32]. Several researchers have employed GEE for AP retrieval [33–39].

A review of the literature reveals that few studies have explored the effectiveness of Sentinel 5 images based on GEE for AP retrieval. A primary focus of Sentinel-5 is the study of air quality and composition-climate interactions with the main data products being O₃, NO₂, SO₂, HCHO, CHOCHO, and aerosols. Furthermore, Sentinel-5 will provide daily global coverage for climate, air quality, and ozone/surface applications of CO, CH₄, and stratospheric O₃ [25–40]. Previous studies also mapped and monitored some specific air pollutants, such as O₃. Therefore, this study aims: (1) to monitor CO, NO₂, SO₂, and O₃ pollutants in Arak city in the period of 2018 and 2019, (2) to evaluate the effectiveness of

Sentinel-5 images for CO, NO₂, SO₂, and O₃ pollutants monitoring, and (3) to explore the efficiency of GEE for AP retrieval.

2. Location of Study Area

Arak city, the capital of the Central Province is located in the central part of Iran (Figure 1). As one of Iran's major manufacturing cities, Arak is widely regarded as one of the four economic poles of the country. This city is the industrial capital of Iran due to the presence of mother industries, the production of 80% of the country's energy equipment, and the presence of the biggest aluminum factory, the biggest manufacturer of heavy machinery in the Middle East, the largest gasoline producer, and the largest mineral industries in the country. As a result, it is one of the most polluted cities in Iran (<https://markazi.doe.ir>, accessed on 1 February 2022). According to the output factors described in Table 1, the fuel consumption of large industries in Arak city and the air pollution caused by this have been estimated based on the available information. Because Arak is one of the most important industrial cores in Iran, fuel consumption in various seasons does not differ significantly from each other [41].

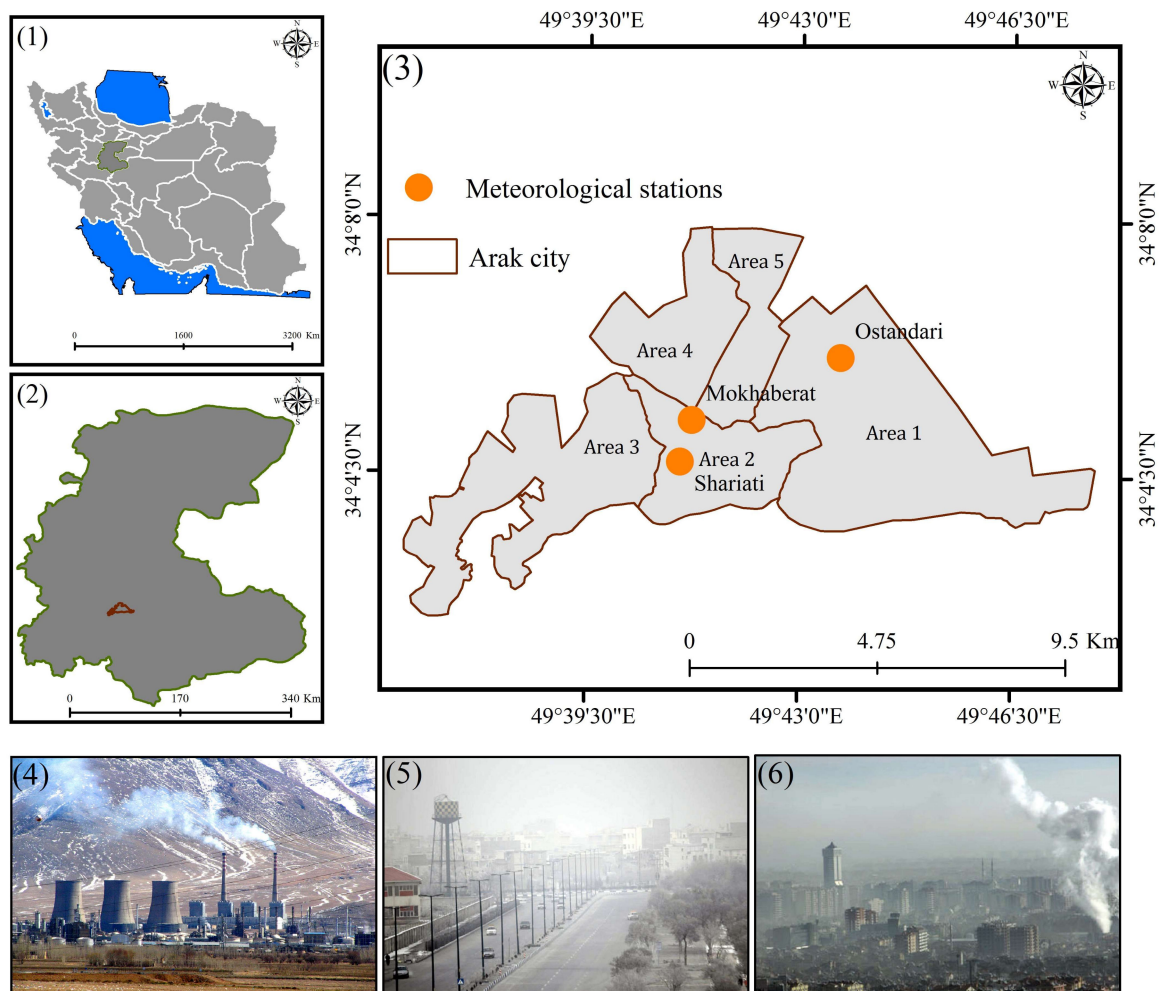


Figure 1. Location of study area, (1) in Iran, (2) Markazi province, and (3) different areas in Arak city. (4–6) are examples of observed air pollution in Arak city.

Table 2 shows that other motor vehicles and heating sources contributed less pollution than industries. As shown in Table 1, industries produced 99% of Arak's air pollution, and the number of pollutants was high as well.

Table 1. Polluting substances in Arak city (in tons per year) caused by fuel consumption in industrial factories.

Fuel Type	Amount in Cubic Meters (m ³)	Carbon Monoxide (CO)	Sulfur Dioxide (SO ₂)	Nitrogen Oxides (NO _x)	Hydrocarbonate (HC)
Kerosene	388,610	22	0.98	0.58	0.13
Fuel oil	12,728,789	6.2	565	88.46	4.15
Gasoline	34,458,613	930	390	15,000	148
Burner fuel	166,195	5.3	3.7	9.1	0.68
Natural gas	2,898,477	780	-	8700	-
Total	50,640,684	1721.7	959.59	10.298	153.140

Table 2. Polluting substances in Arak city (in tons per year) produced by motor vehicles and heating sources.

Contaminating Sources	CO	SO ₂	NO _x	HC
Gasoline cars	12,420	33	190	1536
Motorcycle	10,044	-	-	3487
Diesel cars	3100	15	117	391
Home heating sources	557	297	926	95
Industrial fuel consumption	942,500	959,590	1,606,840	153,140
Refinery production process	314,766	30,707	5823	18,962
Total	1,283,387	990,642	1,613,896	177,611

3. Datasets and Methodology

3.1. Datasets

The main objective of this study was to monitor trends in CO, NO₂, SO₂, and O₃ pollutants in Arak city using time-series Sentinel-5 images derived from GEE. To this end, Sentinel-5 AP were employed to monitor CO, NO₂, SO₂, and O₃ pollutants based on GEE from 2018 to 2019. We also used monthly, seasonal (spring (April, May, and June), summer (July, August, and September), fall (October, November, and December), and winter (January, February, and March)), and annual data on atmospheric pollutants for AP monitoring, collected from the Environmental Organization of Central Province for 2018 and 2019 (Table 3). Figure 1(3) shows the location of pollution monitoring stations in Arak city.

Table 3. The annual air pollution data (ppm) in Ostandari, Shariati, and Mokhaberat stations from 2018 to 2019.

Name of Station	2018			
	CO	NO ₂	SO ₂	O ₃
Ostandari	2.97	22.33	6.15	1.25
Shariati	2.36	16.99	25.38	22.54
Mokhaberat	2.41	2.28	4.18	1.02
	2019			
	CO	NO ₂	SO ₂	O ₃
Ostandari	2.96	2.51	25.14	21.58
Shariati	2.26	15.69	39.29	60.06
Mokhaberat	2.25	22.36	26.78	22.03

3.2. Methodology

To extract pollution maps (CO, NO₂, SO₂, and O₃), the following steps were taken: in the first step, all satellite-based datasets were preprocessed and prepared. Second, results for air pollutants were obtained through JavaScript coding using GEE. As a third step, GEE and Sentinel-5 results were validated based on data from pollution measuring stations. Figure 2 provides a brief review of the methodology used for AP retrieval.

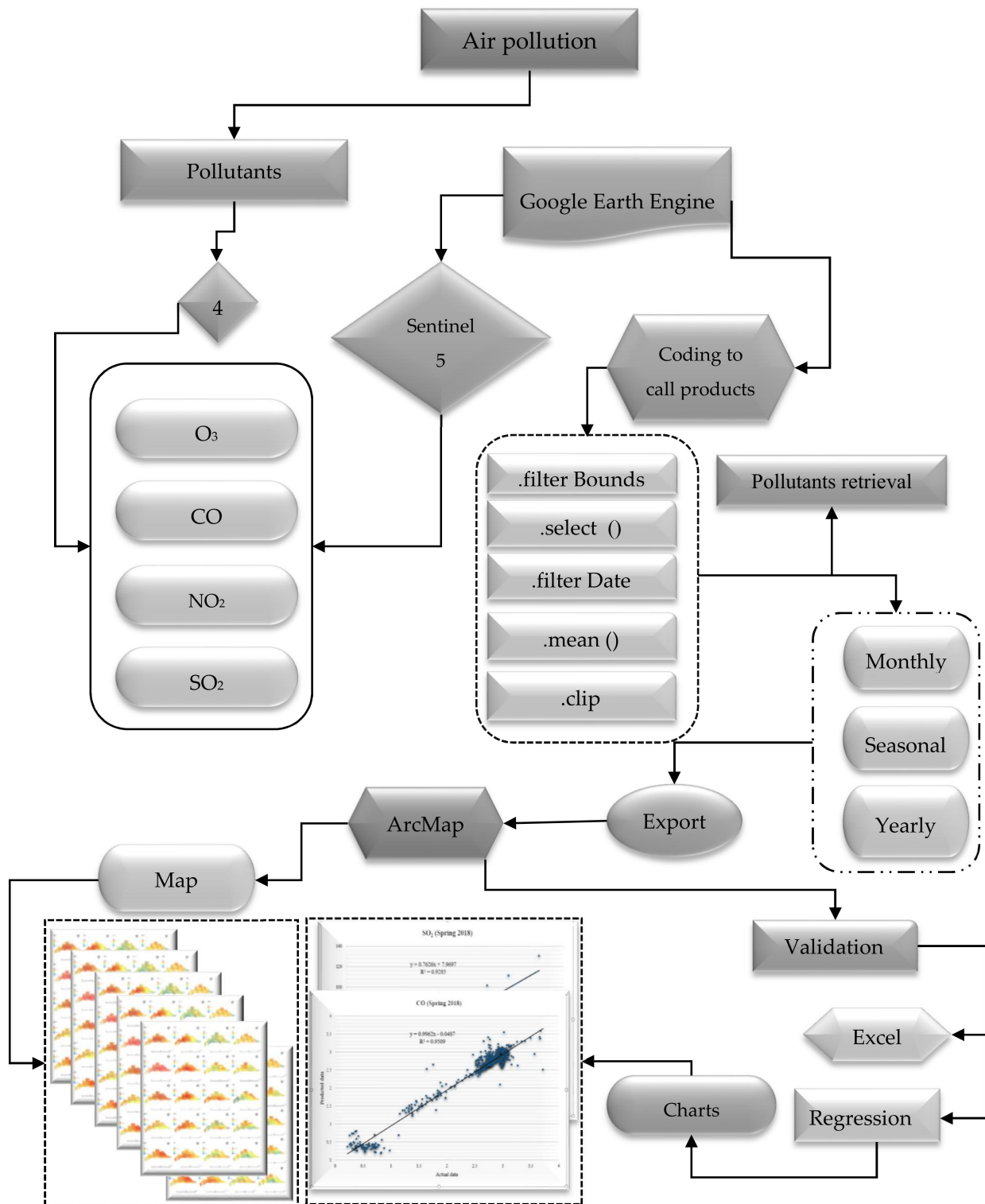


Figure 2. An overview of the methodology used for AP retrieval.

3.2.1. Google Earth Engine (GEE) for AP Retrieval

Google launched GEE in 2010 to store and process Earth observation data in a more reliable and time-efficient way [35]. This platform is valuable when the goal is to process open-access Earth observation data over a large area or long-time interval and in a timely manner [42,43].

To retrieve CO, NO₂, SO₂, and O₃, the Sentinel-5 images were first converted from level 2 to level 3 through the harpconvert tool by the bin spatial operation. Then, after applying the spatial and temporal filters, CO, NO₂, SO₂, and O₃ products from the study area were generated.

Two types of output were then generated, including maps and statistical reports. The results were verified using in situ data obtained from ground-based air pollution stations.

CO Retrieval

The silent killer, CO, is a poisonous and dangerous gas that is odorless, tasteless, and invisible [44]. CO results from the incomplete burning of carbon. As part of Sentinel 5, the CO product is available from 22 November 2018. The features of this product are given in Table 4.

Table 4. Specifications of CO product.

Band Name	Unit	Min	Max	Description
CO_column_number_density	mol/m ²	−297	4.64	CO concentration.
H2O_column_number_density	mol/m ²	−46,536	3.45844 × 10 ⁷	Water vapor column.
Cloud_height	Meter	−8341	5000	Scattered layer height.
Sensor_altitude	Meter	828,542	856,078	Satellite height according to WGS84 geodetic.
Sensor_azimuth_angle	Degree	−180	180	Satellite azimuth angle, East and North WGS84.
Sensor_zenith_angle	Degree	1	66	WGS84 Satellite elevation angle.
Solar_azimuth_angle	Degree	−180	180	Sun azimuth angle, East and North angle WGS84.
Solar_zenith_angle	Degree	9	80	Apex angle of the satellite is the angle away from the vertical.

NO₂ Retrieval

As a result of human activities, especially the burning of fossil fuels, millions of tons of NO₂ are produced every year [45]. In the GEE, NO₂ is one of the Sentinel-5 products that provides offline and in-live high-resolution images. The data on this product can be accessed from 7 October 2018. The features of this product are given in Table 5.

Table 5. Specifications of NO₂ product.

Band Name	Unit	Min	Max	Description
NO ₂ _column_number_density	mol/m ²	−0.0006	0.0096	NO ₂ gradient column density ratio
Tropospheric_NO ₂ _column	mol/m ²	−0.0064	0.0096	Vertical tropospheric column of NO ₂
Stratospheric_NO ₂ _column	mol/m ²	8.7 × 10 ^{−6}	0.0001	Stratospheric NO ₂ vertical column
NO ₂ _slant_column_number	mol/m ²	−51.4 × 10	0.003908	NO ₂ gradient column density
Tropopause_pressure	Pa	0.00644	0.009614	Top pause pressure
Absorbing_aerosol_index	Pa	−14.43	10.67	Aerosol index
Cloud_fraction	fraction	0	1	Effective cloud fraction

Table 5. *Cont.*

Band Name	Unit	Min	Max	Description
Sensor_altitude	Meter	828,543	0.856078	Satellite height according to WGS84 geodetic
Sensor_azimuth_angle	Degree	−180	180	Satellite azimuth angle, East and North WGS84
Sensor_zenith_angle	Degree	0.098	67	WGS84 Satellite elevation angle
Solar_azimuth_angle	Degree	−180	180	Sun azimuth angle, East and North angle WGS84
Solar_zenith_angle	Degree	8	82	Apex angle of the satellite is the angle away from the vertical

SO₂ Retrieval

As presented in Table 6, the GEE has provided a product for the analysis of SO₂. NO₂ data is accessible on the GEE platform from 10 July 2018.

Table 6. Specifications of SO₂ product.

Band Name	Unit	Min	Max	Description
SO ₂ _column_number_density	mol/m ²	−48	0.24	Concentration of vertical column of SO ₂ at ground level.
SO ₂ _column_number_amf	mol/m ²	0.1	3.397	Weighted average of cloudy and clear air mass coefficient.
SO ₂ _slant_column_number	mol/m ²	−0.147	0.162	SO ₂ correction column density column slope.
Cloud_fraction	Fraction	0	1	Effective cloud fraction.
Sensor_azimuth_angle	Degree	−180	180	Satellite azimuth angle, East and North WGS84.
Sensor_zenith_angle	Degree	0.09	67	WGS84 Satellite elevation angle.
Solar_azimuth_angle	Degree	−180	180	Sun azimuth angle, East and North angle WGS84.
Solar_zenith_angle	Degree	8	80	Apex angle of the satellite is the angle away from the vertical.
SO ₂ _column_number_15 km	mol/m ²	0	0	SO ₂ vertical column density at 15 km.

O₃ Retrieval

The role of O₃ in the thermal structure of the Earth and the balance of solar radiation is critical as it prevents ultraviolet radiation from reaching the Earth's surface. However, O₃ is considered a pollutant when its concentration in the lower atmosphere exceeds the air quality standard threshold [46]. The GEE platform has provided a product to monitor and review this critical issue, which provides a set of high-resolution images in real time. This product's data can be accessed from 7 October 2018, whose features are listed in Table 7.

Table 7. Specifications of O₃ product.

Band Name	Unit	Min	Max	Description
O ₃ _column_number_density	mol/m ²	0.025	0.3048	O ₃ between the surface and the top of the atmosphere.
O ₃ _effective_temperature	k	19.92	428.11	Mass coefficient of cloudy and clear air.
Cloud_fraction	Fraction	0	1	The slope of the O ₃ condensation column.
Sensor_azimuth_angle	Degree	−180	180	Satellite azimuth angle, east and north.
Sensor_zenith_angle	Degree	0.098	66.57	WGS84 satellite zenith angle.
Solar_azimuth_angle	Degree	−180	180	Sun azimuth angle, East and North angle WGS84.
Solar_zenith_angle	Degree	8	102	Apex angle of the satellite is the angle away from the vertical.

3.2.2. Accuracy Assessment

Analyzing the accuracy of a retrieval by inversion compared to a standard assumed to be correct is an important step in image analysis. In this regard, median absolute deviation (MAD) [47], mean square error (MSE) [48], root mean square error (RMSE) [49], and mean absolute percentage error (MAPE) [50] statistical analyses were applied to evaluate the accuracy of results for AP retrieval. Equations (1)–(4) describe the MAD, MSE, RMSE, and MAPE operators.

$$MAD = \frac{\sum_{t=1}^n |A_t - F_t|}{n} \quad (1)$$

$$MSE = \frac{\sum_{t=1}^n (A_t - F_t)^2}{n} \quad (2)$$

$$RMSE = \sqrt{\frac{\sum_{t=1}^n (A_t - F_t)^2}{n}} \quad (3)$$

$$MAPE = \frac{\sum_{t=1}^n \left| \frac{A_t - F_t}{A_t} \right|}{n} \times 100 \quad (4)$$

where n is the number of the AP station in the study area, A_t is AP recorded by station, and F_t is AP obtained using the Sentinel-5.

4. Results

Using GEE, pollution parameter maps (CO, NO₂, SO₂, and O₃) were extracted. By coding in JavaScript language in the GEE, four pollution parameters of Sentinel-5 satellite images were called. Using filters, the study years (2018 and 2019) and the location (Arak city) were defined. Following that, images with clouds were filtered by defining cloud filters, and average maps were extracted by defining average filters for both years. The results of the spatiotemporal distribution of CO, NO₂, SO₂, and O₃ in Arak are presented in Figures 3–8 monthly, seasonally, and annually, respectively.

As we can see in Figure 3, for the year 2018, the highest amount of CO was recorded in July and August (0.029 ppm). November was the month with the lowest amount of CO. According to Figure 3, while the highest amount of NO₂ was recorded in December (22.06 ppm), the lowest was recorded in May (12.39 ppm). For SO₂, the highest and lowest amounts were related to July (33.54 ppm) and May (25.14 ppm), respectively, as shown in Figure 3. As we can see in Figure 3, the highest amount of O₃ was recorded in February (0.148 ppm), while the lowest concentrations of O₃ occurred in September and October (0.122 ppm).

According to Figure 4, for the year 2019, the highest amount of CO was recorded in January (0.030 ppm). March was the month with the lowest amount of CO. According to Figure 4, while the highest amount of NO₂ was recorded in January (30.19 ppm), the lowest was recorded in April (11.08 ppm). For SO₂, the highest and lowest amounts were related to October (45.38 ppm), as shown in Figure 4. As we can see in Figure 4, the highest amount of O₃ was recorded in April (0.147 ppm), while the lowest amount of O₃ belonged to November (0.117 ppm).

As we can see in Figure 5, for the year 2018, the seasonal highest amount of CO was recorded in spring and summer (0.028 ppm). According to Figure 5, the highest amount of NO₂ was found in fall (17.39 ppm), and the lowest was found in spring (12.18 ppm). For SO₂, the highest and lowest amounts were related to winter (102.12 ppm) and summer (29.05 ppm), respectively, as shown in Figure 5. As we can see in Figure 5, the highest amount of O₃ was recorded in winter (0.142 ppm), while the lowest amount of O₃ belonged to summer (0.124 ppm).

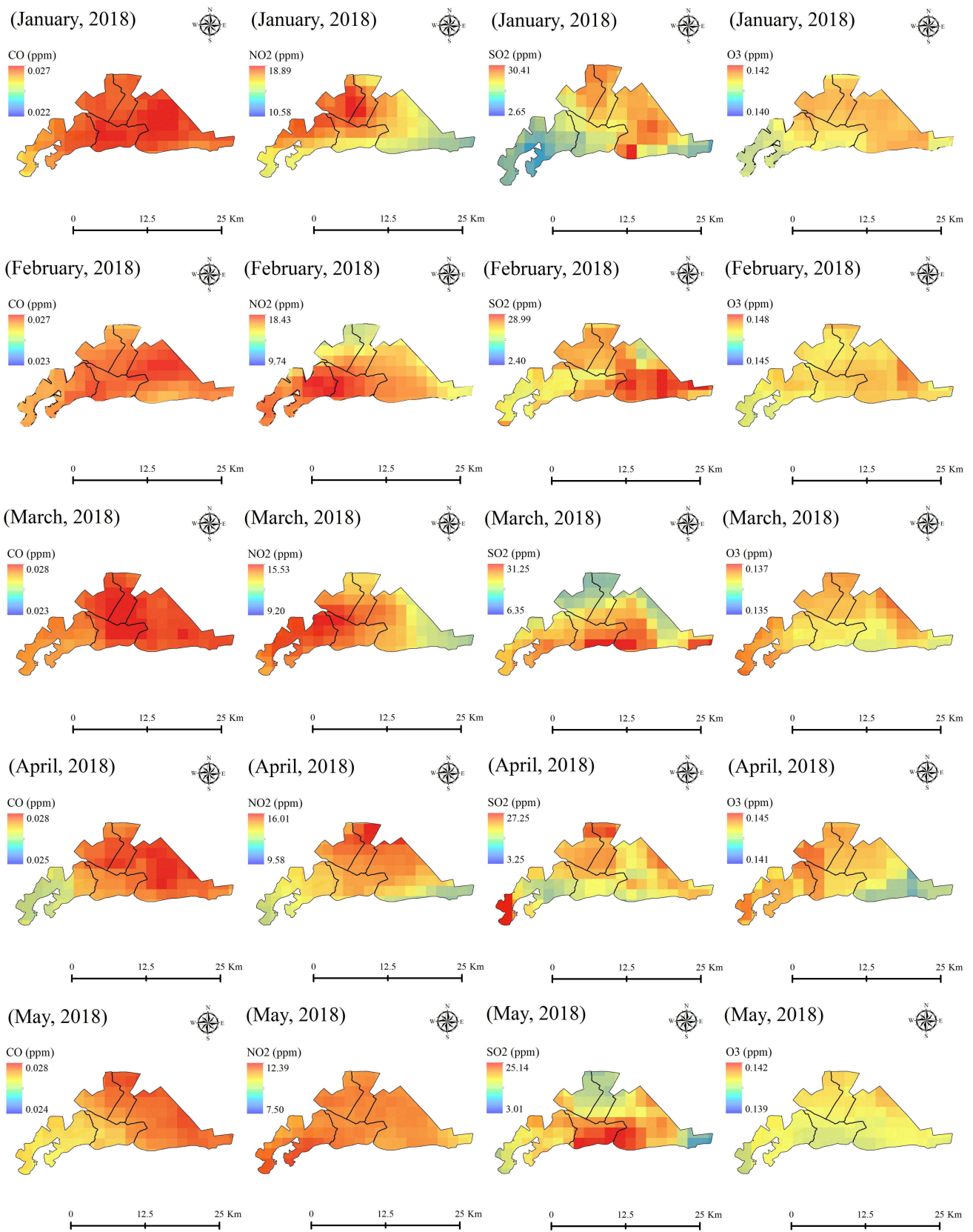


Figure 3. Cont.

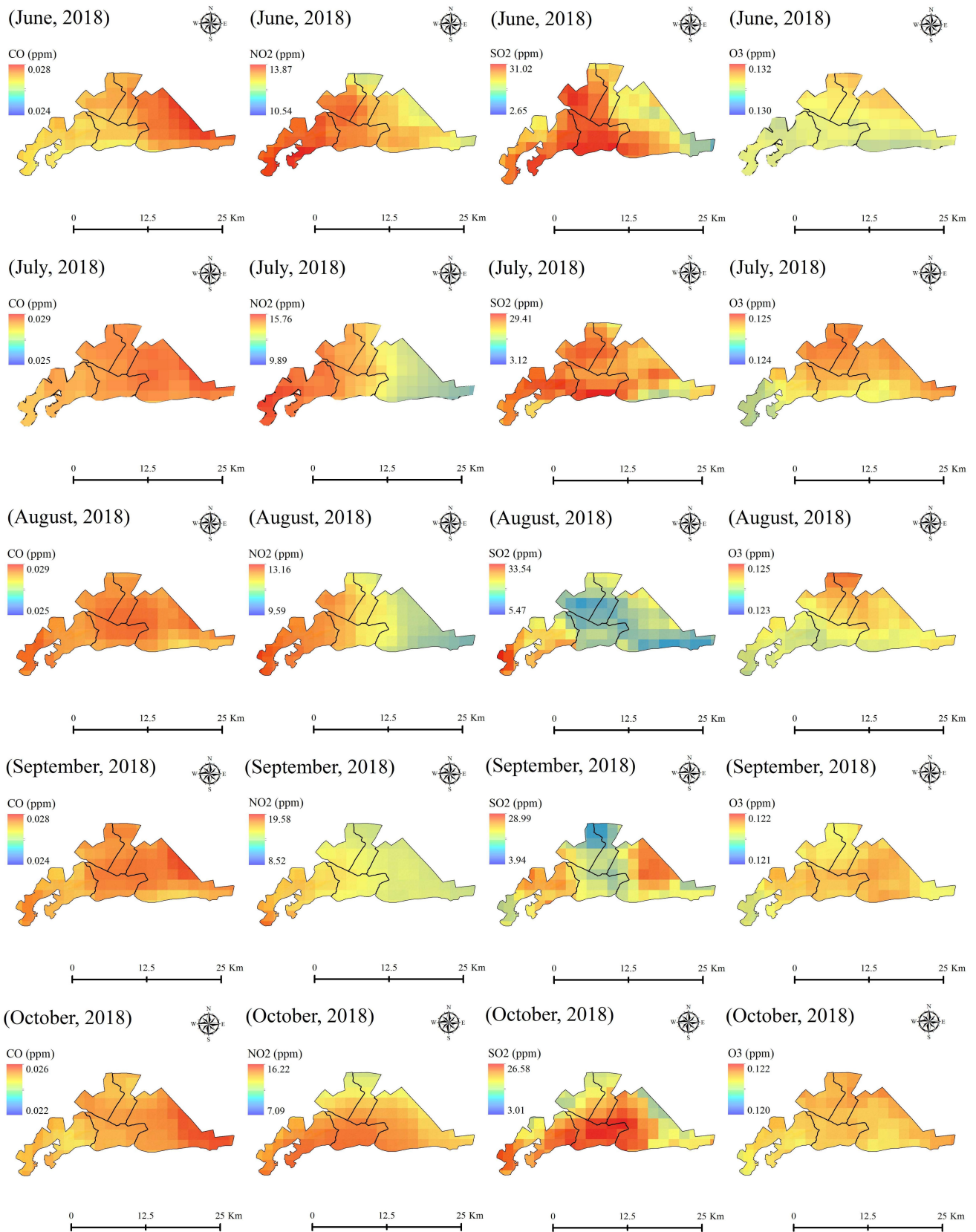


Figure 3. Cont.

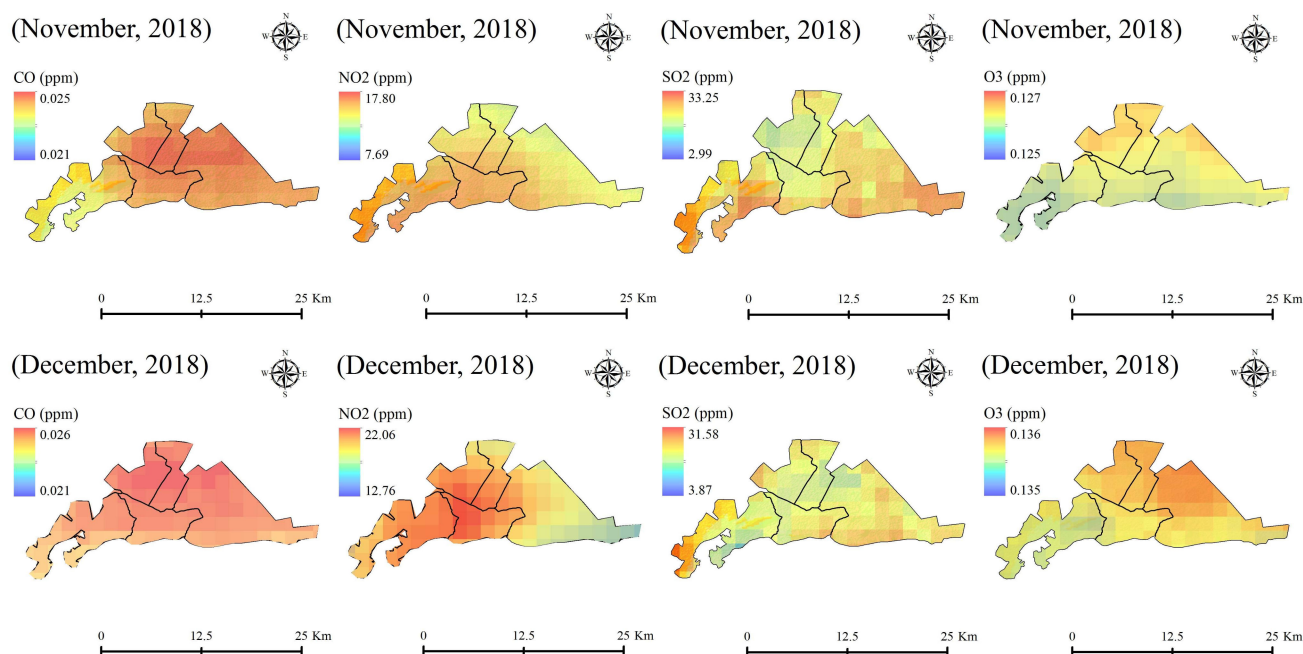


Figure 3. The monthly spatiotemporal distribution of CO, NO₂, SO₂, and O₃ in January, February, March, April, May, June, July, August, September, October, November, and December for the year 2018.

According to Figure 6, for the year 2019, the seasonal highest amount of CO was recorded in spring, summer and winter (0.028 ppm). According to Figure 6, while the highest amount of NO₂ was recorded in winter (21.96 ppm), the lowest amount was recorded in spring (11.66 ppm). For SO₂, the highest and lowest amounts were related to winter (101.25 ppm) and summer (28.01 ppm), respectively, as shown in Figure 6. As we can see in Figure 6, the highest amount of O₃ was recorded in spring (0.136 ppm), while the lowest amount of O₃ was associated with summer and fall (0.122 ppm).

As we can see in Figures 7 and 8, the annual amount of CO was recorded at about 0.027 ppm, which increased (0.030 ppm) in 2019. According to Figures 7 and 8, the highest amount of NO₂ was 13.25 ppm for the year 2018, which increased to about 16.05 ppm in 2019. As we can see in Figures 7 and 8, the annual amount of SO₂ was recorded at 35.60 ppm, which increased to 38.05 ppm in 2019. According to Figures 7 and 8, the highest amount of O₃ in 2018 was 0.133 ppm, which decreased to 0.129 ppm in 2019.

Tables 8 and 9 also show the results of the accuracy assessment for annual and seasonal AP retrieval. Our findings revealed the efficiency of Sentinel-5 AP products based on GEE for mapping and monitoring CO, NO₂, SO₂, and O₃. According to Table 8, the annual CO was estimated with MAD, MSE, RMSE, and MAPE of 0.11, 0.017, 0.13, and 4.16, respectively, for the year 2018. In addition, the annual NO₂ was calculated with MAD of 2.23, MSE of 8.16, RMSE of 2.58, and MAPE of 10.5, as shown in Table 8. As seen in Table 8, the annual SO₂ was estimated with MAD, MSE, RMSE, and MAPE of 4.62, 21.34, 4.62, and 18.20, respectively. Finally, the annual O₃ was calculated with MAD of 2.36, MSE of 5.56, RMSE of 2.36, and MAPE of 10.47, as presented in Table 8.

As we can see in Table 8, the annual CO was estimated with MAD, MSE, RMSE, and MAPE of 0.16, 0.03, 0.17, and 6.75, respectively, for the year 2019. Additionally, the annual NO₂ was calculated with MAD of 2.03, MSE of 5.83, RMSE of 2.41, and MAPE of 9.2, as shown in Table 8. As seen in Table 8, the annual SO₂ was estimated with MAD, MSE, RMSE, and MAPE of 4.31, 18.57, 4.31, and 12.24, respectively. Finally, the annual O₃ was calculated with MAD of 4.6, MSE of 21.16, RMSE of 4.6, and MAPE of 16.99, as shown in Table 8.

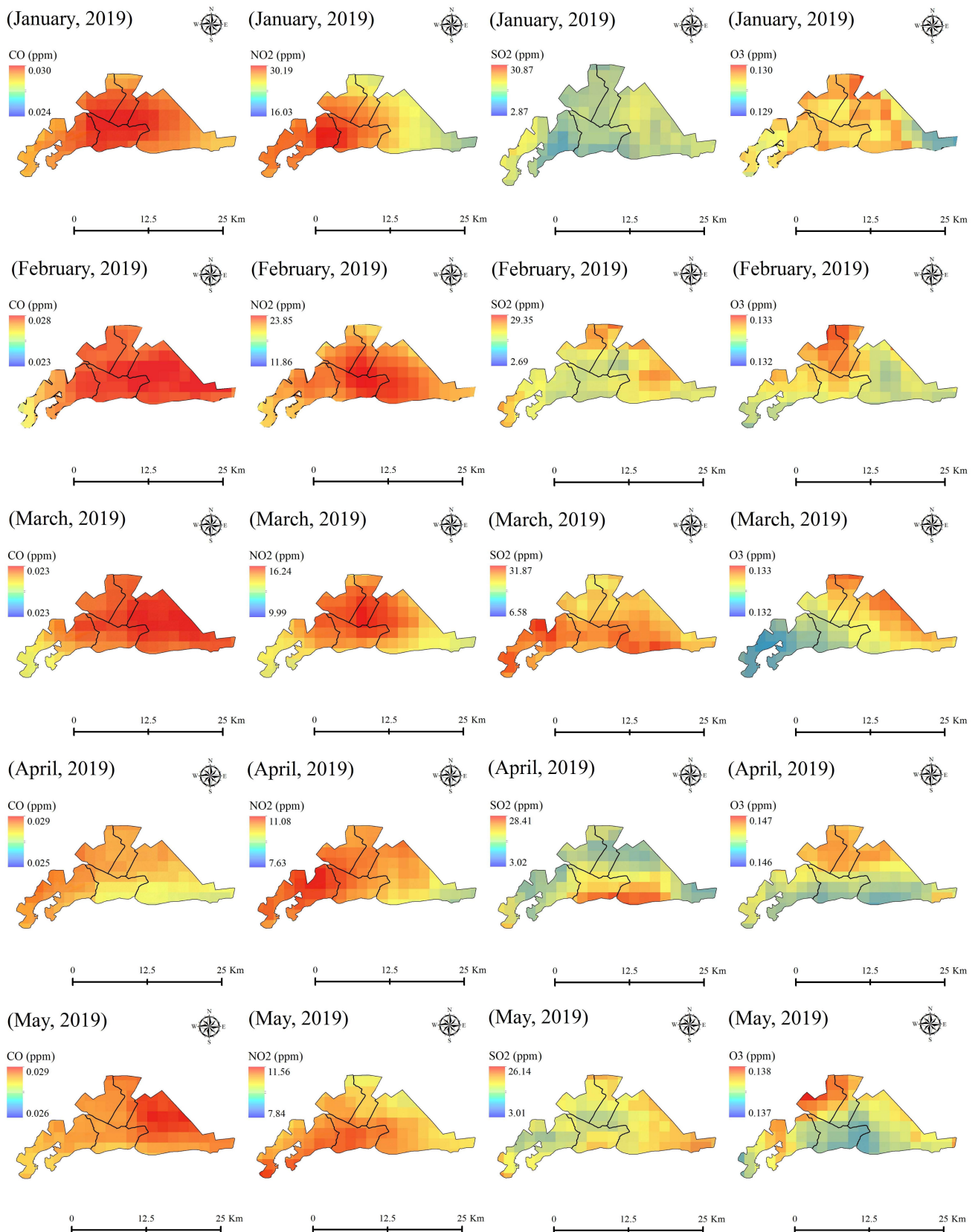


Figure 4. Cont.

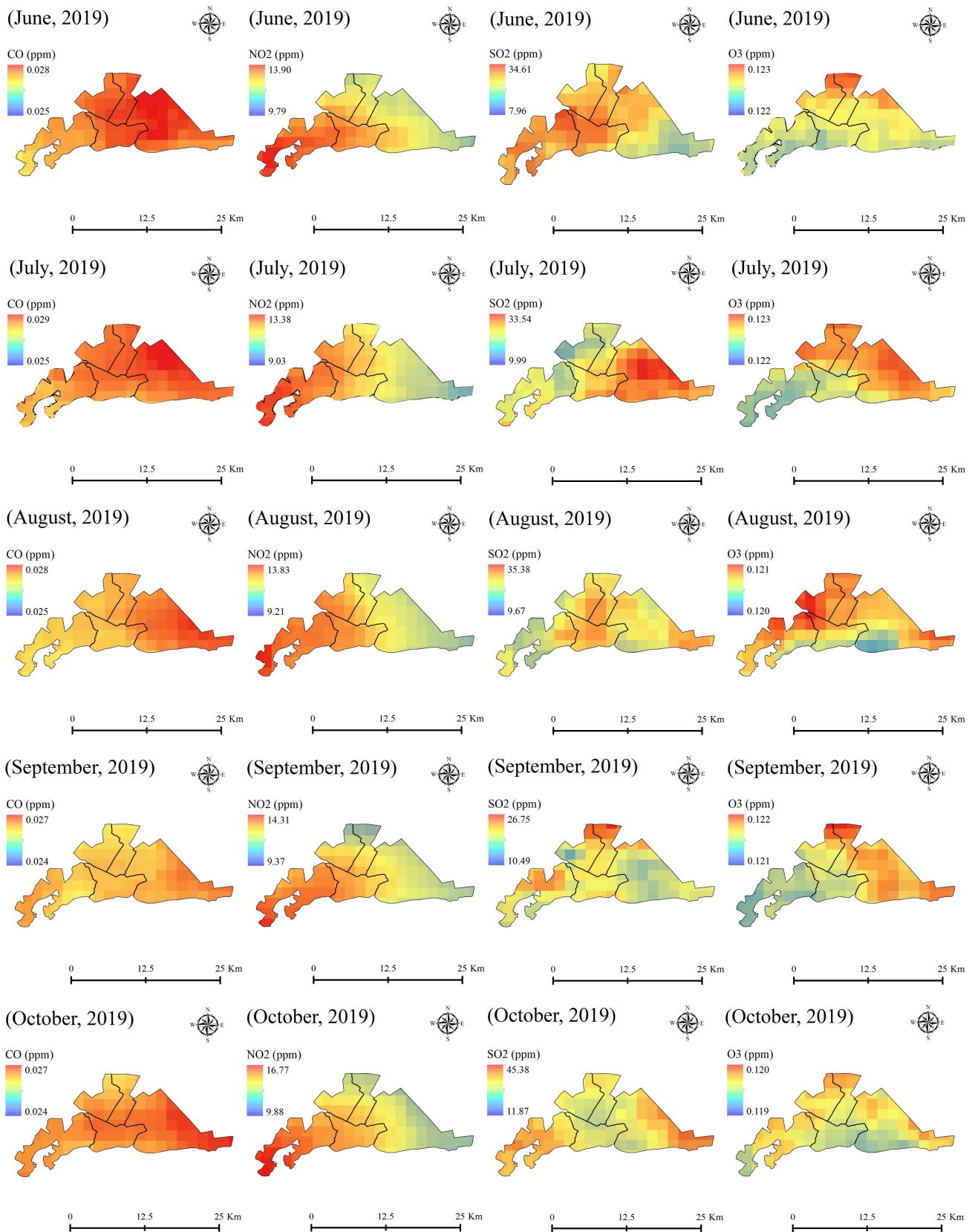


Figure 4. Cont.

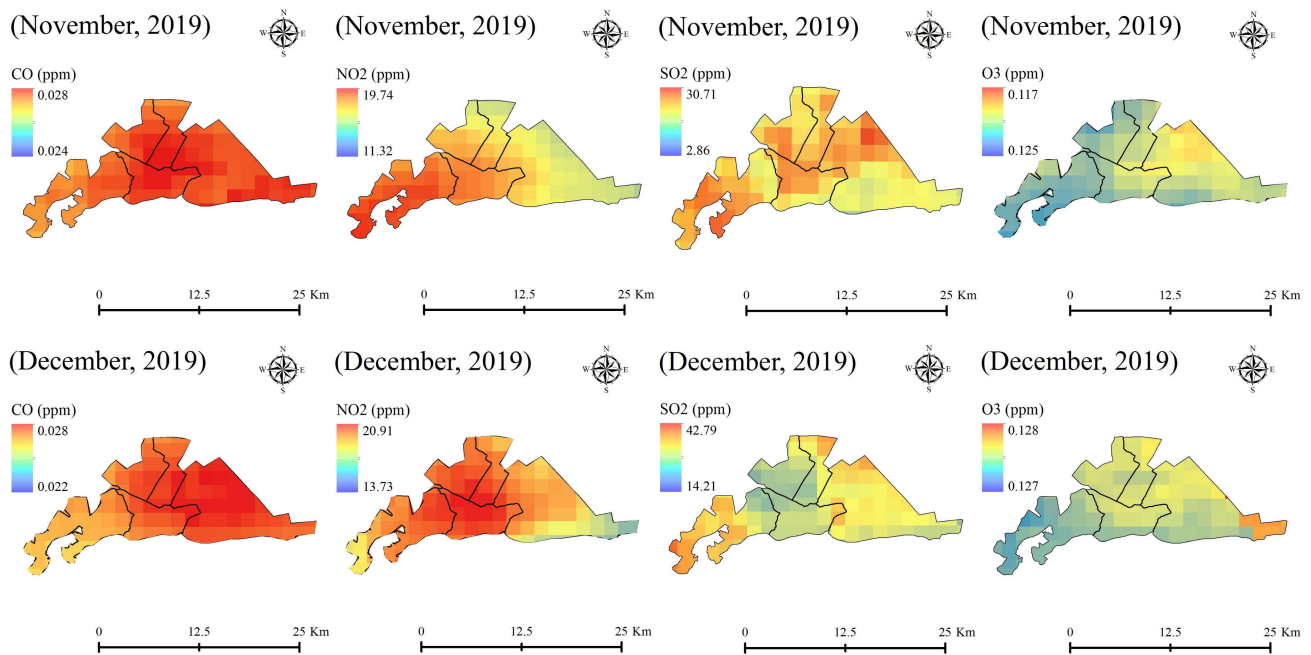


Figure 4. The monthly spatiotemporal distribution of CO, NO₂, SO₂, and O₃ in January, February, March, April, May, June, July, August, September, October, November, and December for the year 2019.

Table 8. The results of accuracy assessment for annual AP retrieval.

Performance metrics	2018			
	CO	NO ₂	SO ₂	O ₃
MAD	0.11	2.23	4.62	2.36
MSE	0.017	8.16	21.34	5.56
RMSE	0.13	2.58	4.62	2.36
MAPE	4.16	10.5	18.20	10.47
2019				
MAD	0.16	2.03	4.31	4.6
MSE	0.03	5.83	18.57	21.16
RMSE	0.17	2.41	4.31	4.6
MAPE	6.75	9.2	12.24	16.99

Table 9. The results of accuracy assessment for seasonal AP retrieval.

Season	Performance metrics	2018				2019			
		CO	NO ₂	SO ₂	O ₃	CO	NO ₂	SO ₂	O ₃
Spring	MAD	0.08	5.22	0.5	4.41	0.11	4.58	1.77	0.72
	MSE	0.08	29.12	0.25	19.44	0.002	24.90	3.13	0.51
	RMSE	0.09	5.39	0.70	7.81	0.12	4.99	1.33	1.27
	MAPE	3.45	22.90	1.60	12.73	1.91	17.97	6.9	2.78
Summer	MAD	0.07	4.57	1.37	1.6	0.11	4.25	0.45	5.84
	MSE	0.012	26.73	1.87	2.56	0.019	27.12	0.20	34.10
	RMSE	0.1	5.17	1.17	2.83	0.11	5.20	0.67	10.35

Table 9. Cont.

Season	Performance metrics	2018				2019			
Fall	MAPE	3.2	19.20	6.32	5.77	4.43	17.67	2.10	32.97
	MAD	0.23	4.21	6.85	1.46	0.043	1.48	1.37	0.15
	MSE	0.08	20.05	46.92	2.13	0.004	3.14	1.87	0.022
	RMSE	0.29	4.47	2.61	2.58	0.069	1.44	1.17	0.26
Winter	MAPE	6.75	19.18	29.58	6.05	1.45	17.76	4.4	0.66
	MAD	0.64	4.22	9.06	1.47	0.43	4.58	0.8	0.82
	MSE	0.60	23.10	82.08	2.16	0.003	27.35	0.64	0.67
	RMSE	0.77	4.80	3.009	2.60	0.055	5.23	0.89	1.45
	MAPE	15.89	17.79	35.17	5.47	1.43	27.28	2.40	6.36

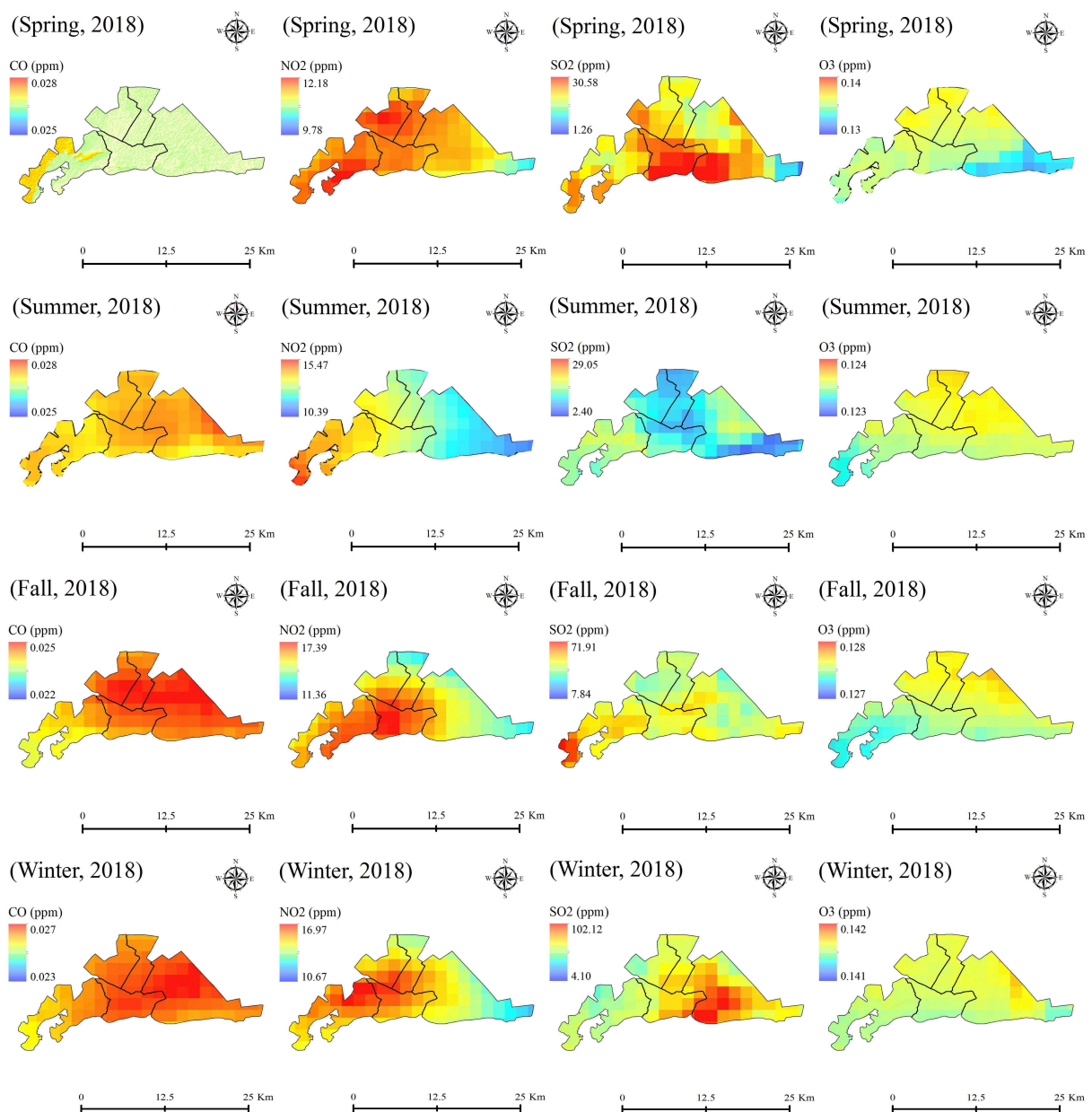


Figure 5. The seasonal spatiotemporal distribution of CO, NO₂, SO₂, and O₃ in Arak for the year 2018 in spring, summer, fall, and winter.

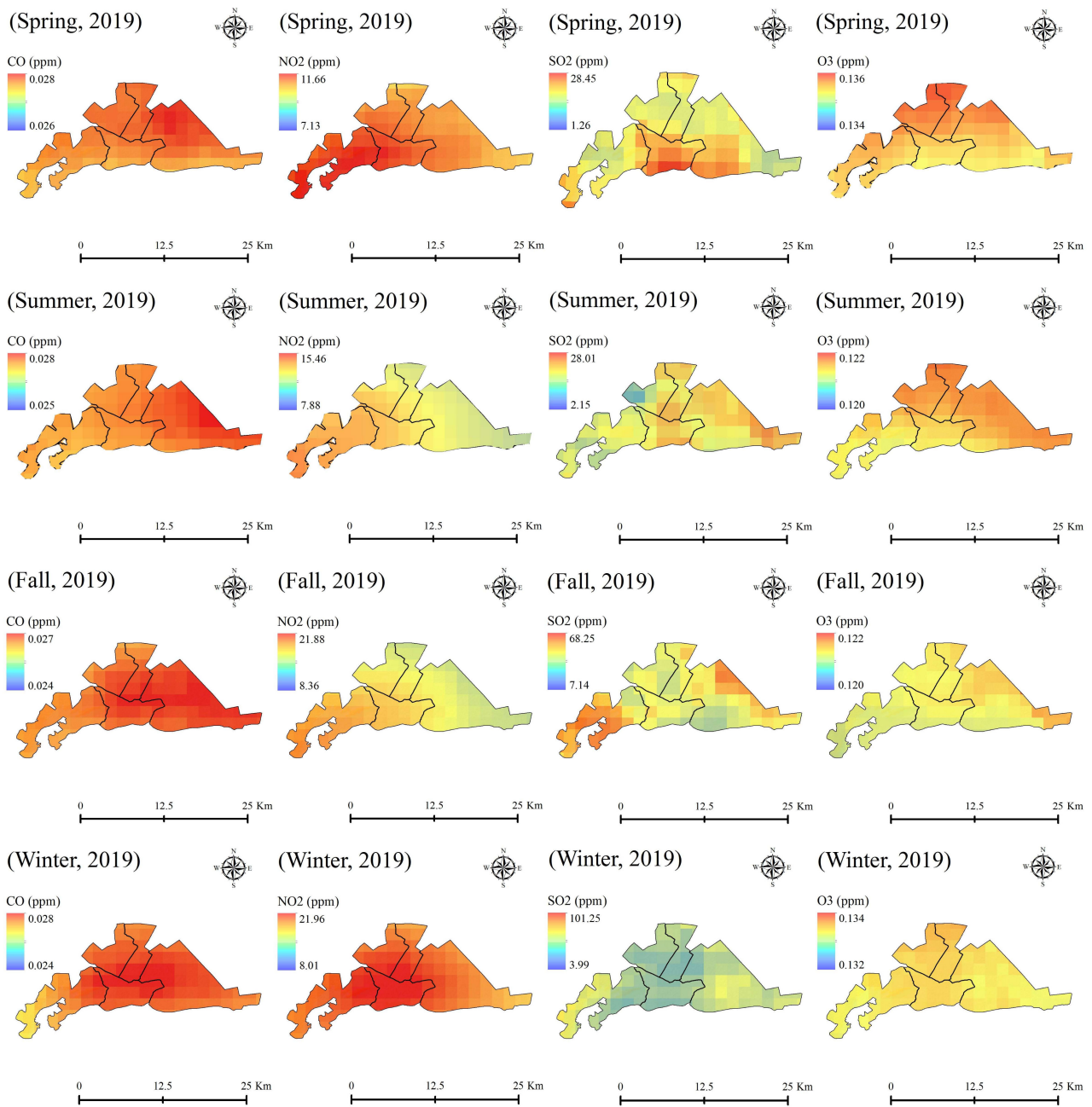


Figure 6. The seasonal spatiotemporal distribution of CO, NO₂, SO₂, and O₃ in Arak for the year 2019 in spring, summer, fall, and winter.

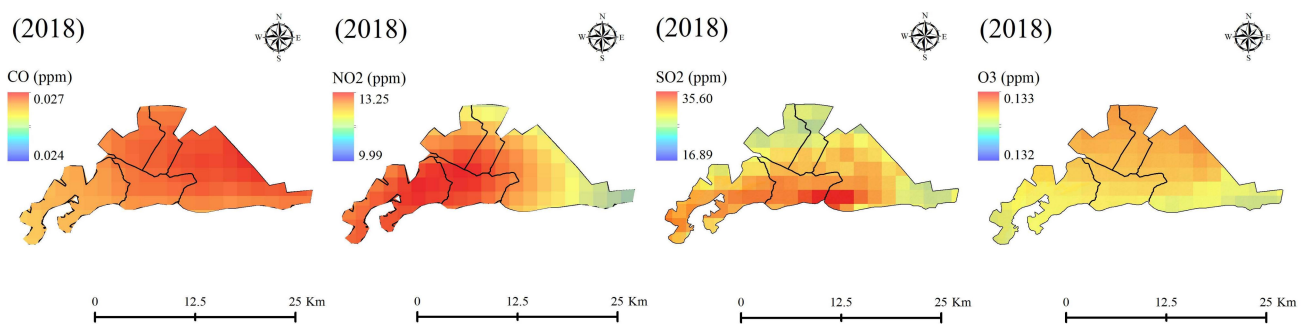


Figure 7. The annual spatiotemporal distribution of CO, NO₂, SO₂, and O₃ in Arak for the year 2018.

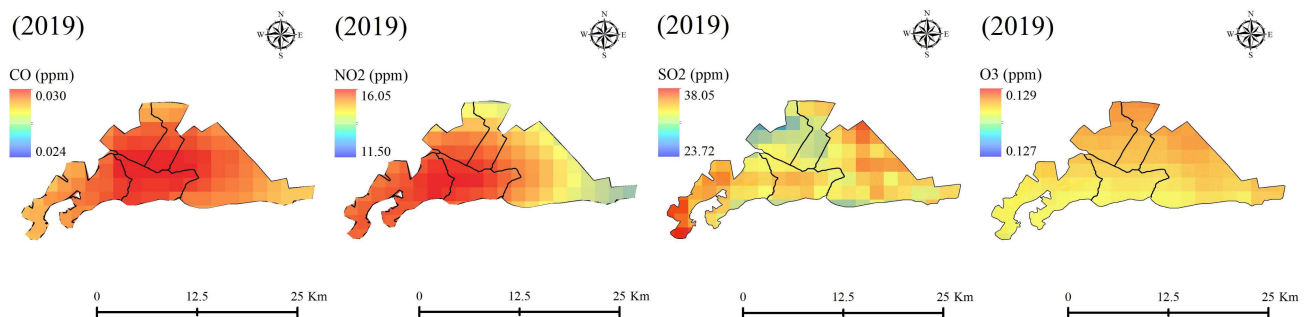


Figure 8. The annual spatiotemporal distribution of CO, NO₂, SO₂, and O₃ in Arak for the year 2019.

Table 9 also shows the results of the accuracy assessment for CO, NO₂, SO₂, and O₃ retrieval. According to Table 9, for spring 2018, the seasonal CO, NO₂, SO₂, and O₃ were estimated with RMSE of 0.09, 5.39, 0.70, and 7.81, respectively. In addition, for summer 2018, the seasonal CO, NO₂, SO₂, and O₃ were calculated with RMSE of 0.1, 5.17, 1.17, and 2.83, respectively, as shown in Table 9. As seen in Table 9, the seasonal CO, NO₂, SO₂, and O₃ were estimated with RMSE of 0.29, 4.47, 2.61, and 2.58, respectively, for fall 2018. Finally, for winter 2018, the seasonal CO, NO₂, SO₂, and O₃ were calculated with RMSE of 0.77, 4.80, 3.009, and 2.60, respectively, as shown in Table 9.

According to Table 9, for spring 2019, the seasonal CO, NO₂, SO₂, and O₃ were estimated with RMSE of 0.12, 4.99, 1.33, and 1.27, respectively. In addition, for summer 2019, the seasonal CO, NO₂, SO₂, and O₃ were calculated with RMSE of 0.11, 5.20, 0.67, and 10.35, respectively, as shown in Table 9. As seen in Table 9, the seasonal CO, NO₂, SO₂, and O₃ were estimated with RMSE of 0.069, 1.44, 1.17, and 0.26, respectively, for fall 2019. Finally, for winter 2019, the seasonal CO, NO₂, SO₂, and O₃ were calculated with RMSE of 0.055, 5.23, 0.89, and 1.45, respectively, as shown in Table 9.

5. Discussion

5.1. General Discussion

From a methodological standpoint, the AP can be computed using two methods: ground-based methods and remote sensing technology. Ground-based methods are the main approach to AP retrieval. These methods, however, are time-consuming and expensive. Additionally, they lack frequent records in dynamic environments, such as cities. Over the last decades, satellite-based models have been employed for AP retrieval. The satellite-based technology is considered an innovative technique that can estimate and monitor AP at dense spatial sampling intervals and large scales. The efficiency of satellite-based data and methods such as the Terra Moderate Resolution Imaging Spectroradiometer (MODIS), the Sentinel-5 Precursor (Sentinel-5P), Global Precipitation Measurement (GPM), Soil Moisture Active and Passive (SMAP), the National Centers for Environmental Prediction (NCEP), Climate Forecast System Reanalysis (CFSR), and the Global Land Data Assimilation System (GLDAS) have proven useful for AP retrieval [12–38]. This study used Sentinel-5 based on GEE to retrieve monthly, annual and seasonal CO, NO₂, SO₂, and O₃ from 2018 to 2019. The results showed that satellite-derived data and applied methods performed well for AP retrieval (Tables 8 and 9). The results of this study revealed that remote sensing technology would make AP mapping and monitoring fast and easier in dynamic areas, such as cities. Our findings also showed a strong correlation coefficient between obtained values from pollution measuring stations and Sentinel-5 (Figures 9–12). According to Figures 5 and 6, the concentration of pollutants in spring 2019 was the same as 2018 for CO and decreased to about 0.52, 2.13, and 0.1 ppm for NO₂, SO₂, and O₃, respectively. The same trend as spring existed for summer 2019 in the concentration of CO, NO₂, and SO₂, as shown in Figures 5 and 6. The concentration of O₃, on the other hand, showed an increase of about 0.02 ppm in summer 2019 compared to summer 2018. As we can see in Figures 5 and 6, while the concentration of CO and NO₂ increased by

about 0.002 and 4.49 ppm, respectively, from 2018 to 2019 in fall, the concentration of SO₂ and O₃ decreased by about 3.63 and 0.006 ppm from 2018 to 2019, respectively. The concentration of CO and NO₂ increased by about 0.001 and 4.99 ppm, respectively, from 2018 to 2019 in winter. The concentration of SO₂ and O₃, however, decreased by about 0.87 and 0.008 ppm, respectively, from 2018 to 2019 in this season. In the domain of the annual concentration of pollutants, there was an increase of 0.003, 2.08, and 2.45 ppm for CO, NO₂, and SO₂, respectively, from 2018 to 2019, as shown in Figures 7 and 8. However, a decrease of 0.004 ppm in the domain of O₃ concentration was observed, according to Figures 7 and 8.

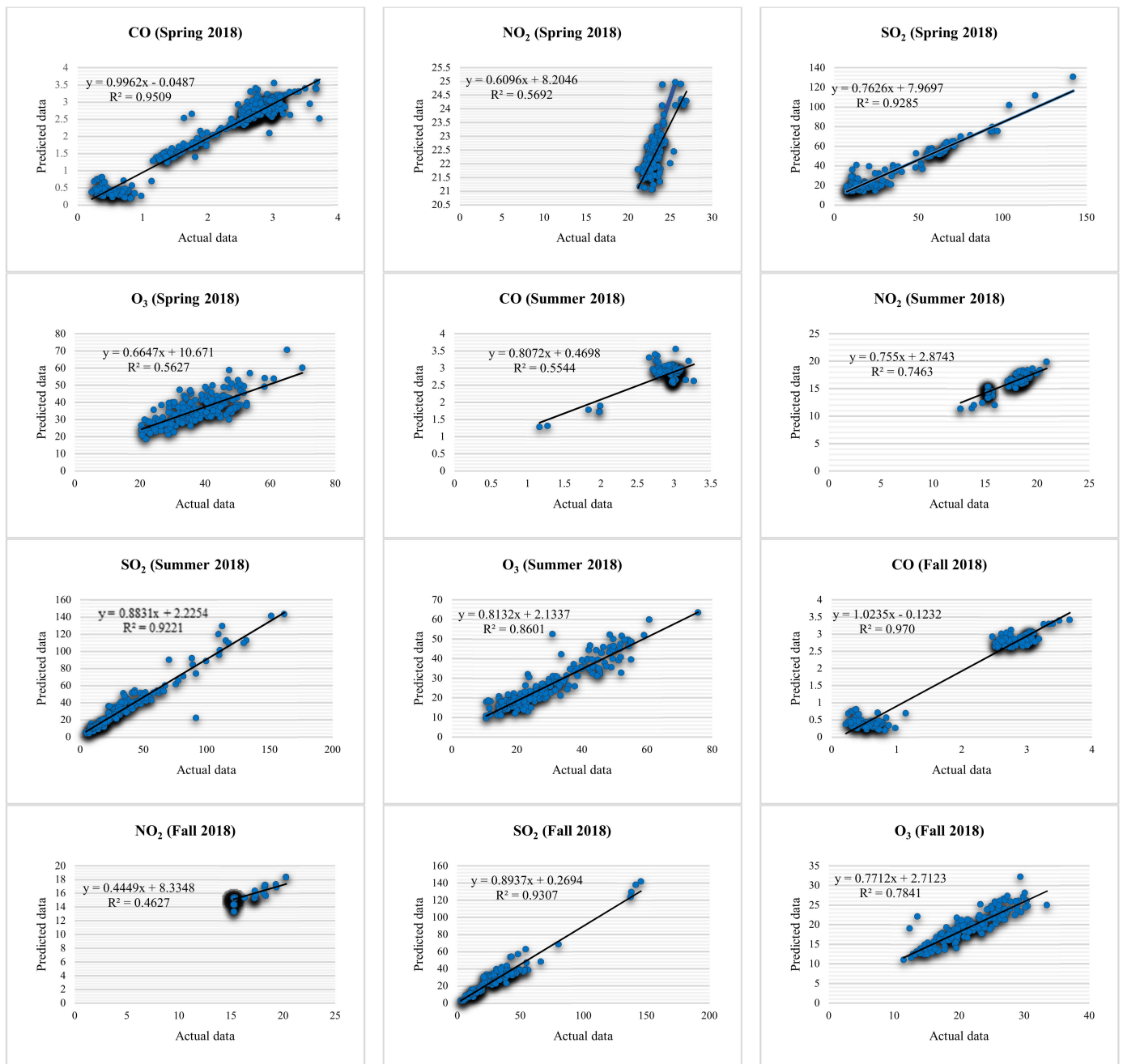


Figure 9. Cont.

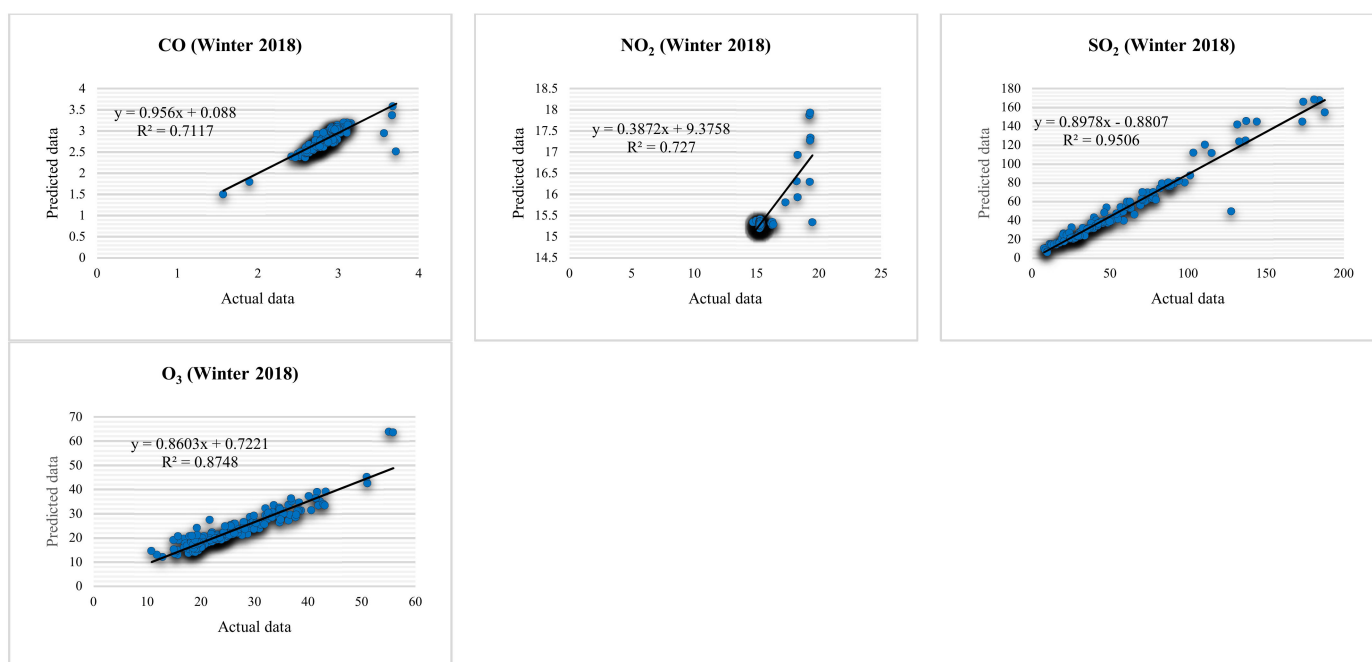


Figure 9. Linear regression correlation between seasonal CO, NO₂, SO₂, and O₃ obtained using Sentinel-5 (predicted data) and pollution measuring stations (actual data) for the year 2018.

According to Figure 9, the correlation coefficients (R^2) for CO, NO₂, SO₂, and O₃ in spring 2018 were 0.9509, 0.5692, 0.9285, and 0.5627, respectively. The correlation coefficients between the data obtained from Sentinel-5 and the ground data for summer 2018 were 0.5544, 0.7463, 0.9221, and 0.8601 for CO, NO₂, SO₂, and O₃, respectively, as shown in Figure 9. According to Figure 9, strong correlation coefficients of 0.970, 0.4627, 0.9307, and 0.7841 were found for CO, NO₂, SO₂, and O₃, respectively, in fall 2018. In addition, the correlation coefficients between the data obtained from Sentinel-5 and the ground data for winter 2018 were 0.7117, 0.727, 0.9506, and 0.8748 for CO, NO₂, SO₂, and O₃, respectively, as shown in Figure 9. In general, strong correlation coefficients were estimated between data obtained from remote sensing technology and ground-based data in all seasons, in particular winter for the year 2018. The results of this research are in accordance with reports received from the Environmental Organization of Central Province (<https://markazi.doe.ir>, accessed on 1 February 2022).

According to Figure 10, the correlation coefficients for CO, NO₂, SO₂, and O₃ in spring 2019 were 0.8974, 0.6174, 0.8959, and 0.5192, respectively. The correlation coefficients between the data obtained from Sentinel-5 data and the ground data for summer 2019 were 0.92, 0.855, 0.8391, and 0.8298 for CO, NO₂, SO₂, and O₃, respectively, as shown in Figure 10. According to Figure 10, strong correlation coefficients of 0.917, 0.6275, 0.9326, and 0.8197 were found for CO, NO₂, SO₂, and O₃, respectively, in fall 2019. In addition, the correlation coefficients between the data obtained from Sentinel-5 and the ground data for winter 2019 were 0.9009, 0.9471, 0.8933, and 0.8332 for CO, NO₂, SO₂, and O₃, respectively, as shown in Figure 10. In sum, the results of the correlation coefficients between the predicted data from remote sensing technology and actual data received from pollution measuring stations demonstrated a difference (about <0.6) from 2018 to 2019 in all seasons. This difference could be because of some missing data received from pollution measuring stations.

From Figure 11, it can be seen that strong correlation coefficients of 0.9509, 0.9344, 0.9344, and 0.8376 for CO, NO₂, SO₂, and O₃, respectively, were obtained in 2018.

According to Figure 12, strong correlation coefficients of 0.9103, 0.8558, 0.9078, and 0.8133 were found for CO, NO₂, SO₂, and O₃, respectively, in 2019.

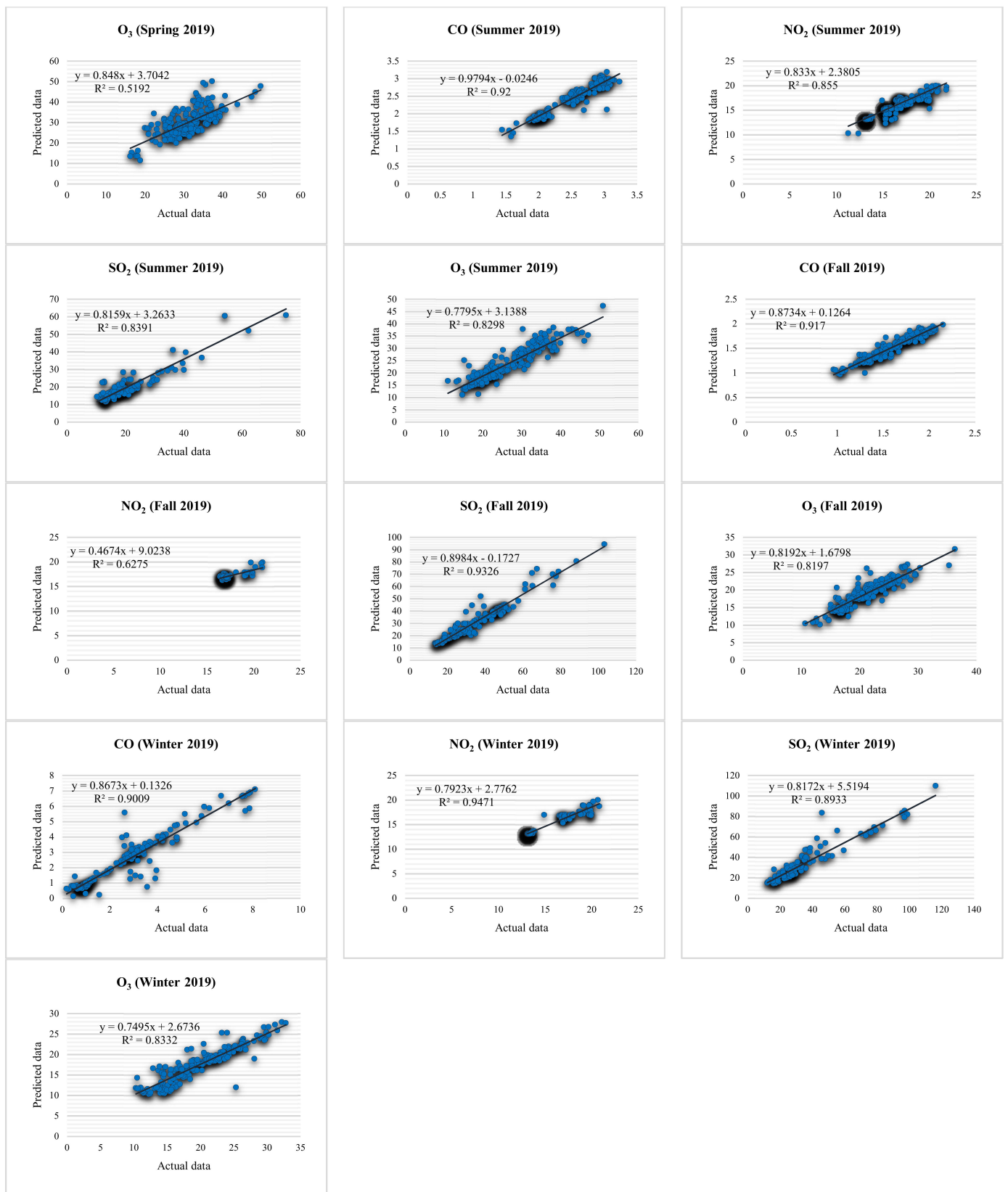


Figure 10. Linear regression correlations between seasonal CO, NO₂, SO₂, and O₃ obtained using Sentinel-5 (predicted data) and pollution measuring stations (actual data) for the year 2019.

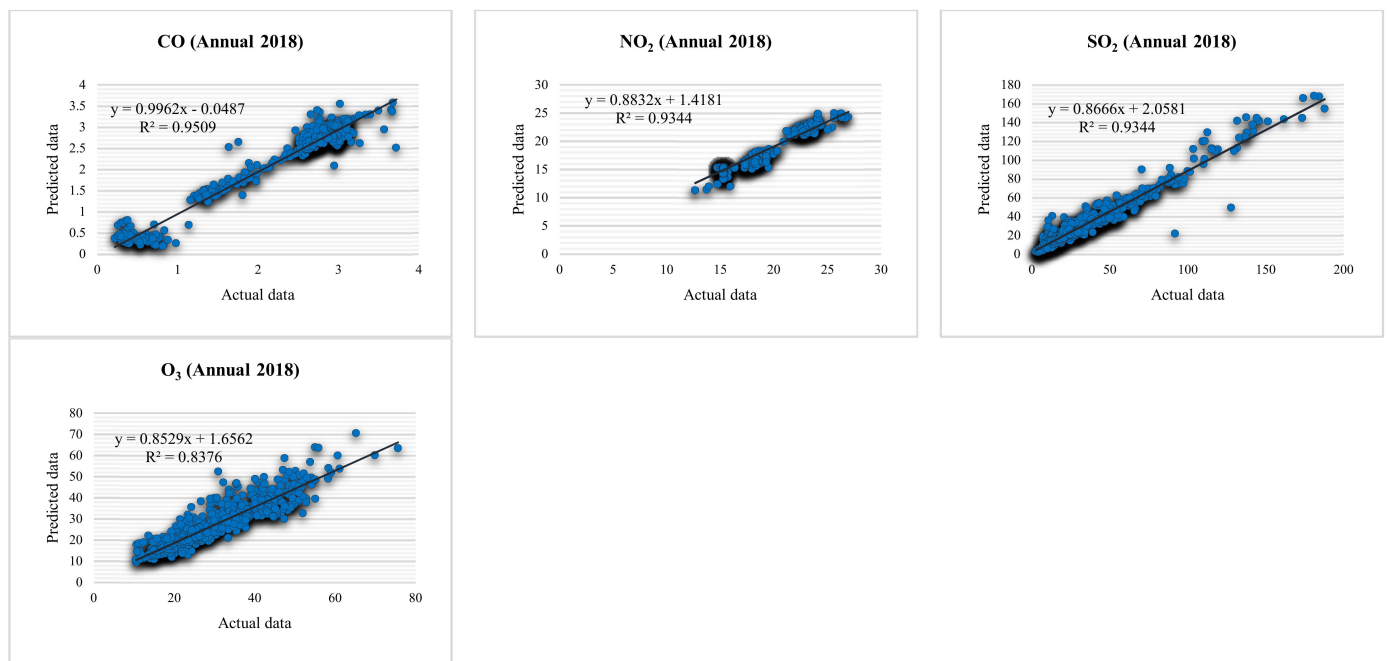


Figure 11. Linear regression correlations between annual CO, NO₂, SO₂, and O₃ obtained using Sentinel-5 (predicted data) and pollution measuring stations (actual data) for the year 2018.

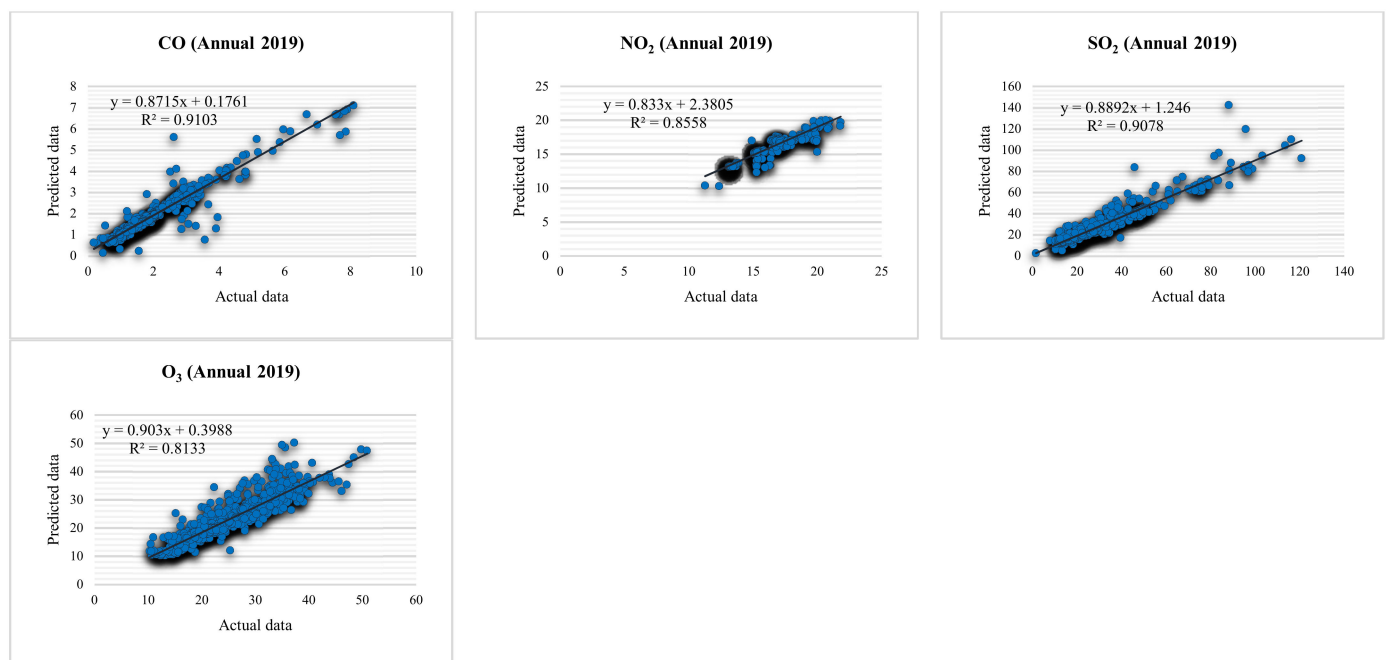


Figure 12. Linear regression correlations between annual CO, NO₂, SO₂, and O₃ obtained using Sentinel-5 (predicted data) and pollution measuring stations (actual data) for the year 2019.

5.2. Monthly Distribution of AP in 2018 and 2019

Detailed zoning maps of Arak in 2018 showed that the most polluted areas were in the city's center (Areas 4 and 5), while the least polluted area was 3, which is in accordance with reports received from the Environmental Organization of Central Province (Figure 3). Using satellite images, it was found that the least pollution was recorded in area 3 due to the presence of vegetation and the surrounding gardens. However, the highest distribution of pollution occurred in area 1, which was due to the location of all small and large industries of Arak city in this area, in accordance with collected data from air pollution

measuring stations. According to Figure 3, the highest concentration of CO occurred in July and August (0.029 ppm) for the year 2018. The highest concentration of NO₂ was also estimated for December (22.06 ppm). The highest concentration of SO₂ occurred in August (33.54 ppm). The highest value for O₃ was estimated in February, as shown in Figure 3.

The pollution zoning maps for Arak city in 2019 showed the highest levels of pollution in areas 1 and 2, and the least levels of pollution in area 3 (Figure 4). Based on the distribution of pollution using satellite images, it was found that area 3 had the least pollution. This was due to the excellent vegetation and the surrounding gardens. However, area 1 had the highest pollution, which was due to the location of all small and large industries of Arak city in this area, which is in accordance with data received from the Environmental Organization of Central Province. As we can see in Figure 4, the highest concentration of CO occurred in January (0.030 ppm) for the year 2019. The highest concentration of NO₂ was also estimated for January (30.19 ppm), while the highest concentration of SO₂ belonged to October (45.38 ppm). The highest value for O₃ was estimated in April (0.147 ppm), as shown in Figure 4.

5.3. The Effect of Land Use on Air Pollution in Arak City

Based on an analysis of land use and its effect on air pollution, it was found that the most polluted area was the Arak industrial town, which is located in area 1. It has been reported that the industrial factories of Arak play a significant role in the air pollution of Arak city by producing suspended particles, carbonaceous oxides, nitrogenous oxides, ammonia, etc. [41]. The least air pollution was found in area 3 due to the high density of vegetation, which is in accordance with the identified green areas on the land use map.

Arak is surrounded by hills and the city's highlands are located to the south and the city's industrial area is to the southeast. The prevailing winds in this area are from the west and southwest. Regardless of other natural factors, due to the average speed (between 7 and 10 K/H) of the prevailing winds, pollution from the industries in the east of this city cannot penetrate into the residential areas [51]. Due to the topography, the south and west of Arak city are surrounded by highlands, and, since local winds are typically from the east and northeast, this factor, as well as the fact that January and April are the months with the greatest percentage of still air, contributed to creating an inversion, which is in accordance with reports received from the Environmental Organization of Central Province.

5.4. Limitation of the Study

Although satellite images are a promising source of data for generating estimates at high spatial resolution on a local scale as they capture some spatial variability, they are limited to generalizing in certain areas [52,53]. Future work should focus on combining additional datasets that are readily available globally (e.g., additional bands of satellite data, normalized difference vegetation index (NDVI)/enhanced vegetation index (EVI), meteorology, digital elevation model (DEM)) that can be combined with meter-scale satellite images to generate better estimates of air pollutants. In addition, future efforts will need to assess the sensitivity of image-based models to images collected with different temporal aspects, such as time of day and season.

6. Conclusions

Recent progress in Earth observation technology, and remote sensing in particular, has turned remote sensing into big data technology, which demands efficient, effective, and cost-effective data-driven methods. Therefore, applying different data-driven approaches and comparing their efficiency can be considered as the state of the art for remote sensing sciences which is the object of the current research. This study employed Sentinel-5 images based on GEE to retrieve CO, NO₂, SO₂, and O₃ parameters. According to our findings, Sentinel-5 images based on GEE turned out to be the most efficient approach for AP retrieval. This study also confirmed a strong correlation between CO, NO₂, SO₂, and O₃ retrieved from Sentinel-5 and air pollution stations.

Our findings confirm that GEE is appropriate to exploit vast amounts of data, and that it can be regarded as a testbed for machine learning algorithms. In the investigation of air pollution in urban areas, satellite images in both time and space can provide optimal management and high accuracy. Considering the fact that most pollution monitoring station data are incomplete due to malfunctioning devices, AP classification from remote sensing images is a challenging task because of the wide range of features that can cause heterogeneity. The present study addresses this complexity by utilizing an automated data-driven platform. This study proves the applicability of Sentinel-5 in GEE for providing a general framework for the monitoring of CO, NO₂, SO₂, and O₃ at various levels and scales. The results of this study contribute to monitoring programs for CO, NO₂, SO₂, and O₃ changes in dynamic environments, such as cities. The results are readily generalizable to more complex Earth feature monitoring.

Author Contributions: Conceptualization, M.K.G.; data curation, H.R. and M.S.; formal analysis, G.L.; investigation, N.M.; methodology, M.K.G., H.R., N.M. and B.S.; software, M.K.G., M.S. and B.S.; supervision, G.L.; validation, G.L.; writing—original draft, M.K.G.; writing—review and editing, G.L. All authors have read and agreed to the published version of the manuscript.

Funding: This research received no external funding.

Institutional Review Board Statement: Not applicable.

Informed Consent Statement: Not applicable.

Data Availability Statement: The data presented in this study are available upon request from the corresponding author.

Conflicts of Interest: The authors declare no conflict of interest.

References

1. Pope, C.A., III; Lefler, J.S.; Ezzati, M.; Higbee, J.D.; Marshall, J.D.; Kim, S.-Y.; Bechle, M.; Gilliat, K.S.; Vernon, S.E.; Robinson, A.L. Mortality risk and fine particulate air pollution in a large, representative cohort of US adults. *Environ. Health Perspect.* **2019**, *127*, 077007. [[CrossRef](#)] [[PubMed](#)]
2. Wang, Y.; Bechle, M.J.; Kim, S.-Y.; Adams, P.J.; Pandis, S.N.; Pope III, C.A.; Robinson, A.L.; Sheppard, L.; Szpiro, A.A.; Marshall, J.D. Spatial decomposition analysis of NO₂ and PM_{2.5} air pollution in the United States. *Atmos. Environ.* **2020**, *241*, 117470. [[CrossRef](#)]
3. Bakhshi Lomer, A.R.; Rezaeian, M.; Rezaei, H.; Lorestani, A.; Mijani, N.; Mahdad, M.; Raeisi, A.; Arsanjani, J.J. Optimizing Emergency Shelter Selection in Earthquakes Using a Risk-Driven Large Group Decision-Making Support System. *Sustainability* **2023**, *15*, 4019. [[CrossRef](#)]
4. Zhou, B.; Zhang, S.; Xue, R.; Li, J.; Wang, S. A review of Space-Air-Ground integrated remote sensing techniques for atmospheric monitoring. *J. Environ. Sci.* **2023**, *123*, 3–14. [[CrossRef](#)] [[PubMed](#)]
5. Bakaeva, N.; Le, M.T. Determination of urban pollution islands by using remote sensing technology in Moscow, Russia. *Ecol. Inform.* **2022**, *67*, 101493. [[CrossRef](#)]
6. Saffarzadeh, M.; Rezaei, H.; Majidi, M.Z. A Pricing Model for Freeway Tolls Based on the Share of Mode Shift, Route Shift, Travel Time Change and Users' Willingness to Pay (Case study: Tehran-Saveh Freeway). *J. Transp. Res.* **2022**, *19*, 359–370.
7. Ialongo, I.; Virta, H.; Eskes, H.; Hovila, J.; Douros, J. Comparison of TROPOMI/Sentinel-5 Precursor NO₂ observations with ground-based measurements in Helsinki. *Atmos. Meas. Tech.* **2020**, *13*, 205–218. [[CrossRef](#)]
8. Amani, M.; Ghorbanian, A.; Ahmadi, S.A.; Kakooei, M.; Moghimi, A.; Mirmazloumi, S.M.; Moghaddam, S.H.A.; Mahdavi, S.; Ghahremanloo, M.; Parsian, S. Google earth engine cloud computing platform for remote sensing big data applications: A comprehensive review. *IEEE J. Sel. Top. Appl. Earth Obs. Remote Sens.* **2020**, *13*, 5326–5350. [[CrossRef](#)]
9. Rezaei, H.; Irannezhad, E.; Mamdoohi, A.R. Heterogeneous analysis of mode choice behavior using latent class model. *J. Transp. Res.* **2021**, *18*, 61–74.
10. Aghashariatmadari, Z. The effects of COVID-19 pandemic on the air pollutants concentration during the lockdown in Tehran, Iran. *Urban Clim.* **2021**, *38*, 100882. [[CrossRef](#)]
11. Mamdoohi, A.R.; Rezaei, H.; Irannezhad, E.; Saffarzadeh, A.; Abbasi, M. Hour-and Period-based congestion pricing, case of Tehran mode choice. *Q. J. Transp. Eng.* **2022**, *14*, 54.
12. Sari, N.M.; Kuncoro, M.N.S. Monitoring of CO, NO₂ and SO₂ Levels During the COVID-19 Pandemic in Iran Using Remote Sensing Imagery. *Geogr. Environ. Sustain.* **2021**, *14*, 183–191. [[CrossRef](#)]
13. Ghaffarpasand, O.; Ropkins, K.; Beddows, D.C.; Pope, F.D. Detecting high emitting vehicle subsets using emission remote sensing systems. *Sci. Total Environ.* **2023**, *858*, 159814. [[CrossRef](#)]

14. Filonchik, M.; Yan, H.; Yang, S.; Lu, X. Detection of aerosol pollution sources during sandstorms in Northwestern China using remote sensed and model simulated data. *Adv. Space Res.* **2018**, *61*, 1035–1046. [[CrossRef](#)]
15. Batur, I.; Markolf, S.A.; Chester, M.V.; Middel, A.; Hondula, D.; Vanos, J. Street-level heat and air pollution exposure informed by mobile sensing. *Transp. Res. Part D Transp. Environ.* **2022**, *113*, 103535. [[CrossRef](#)]
16. Schaefer, M.; Salari, H.E.; Köckler, H.; Thinh, N.X. Assessing local heat stress and air quality with the use of remote sensing and pedestrian perception in urban microclimate simulations. *Sci. Total Environ.* **2021**, *794*, 148709. [[CrossRef](#)]
17. Garajeh, M.K.; Feizizadeh, B. A comparative approach of data-driven split-window algorithms and MODIS products for land surface temperature retrieval. *Appl. Geomat.* **2021**, *13*, 715–733. [[CrossRef](#)]
18. Mukundan, A.; Huang, C.-C.; Men, T.-C.; Lin, F.-C.; Wang, H.-C. Air Pollution Detection Using a Novel Snap-Shot Hyperspectral Imaging Technique. *Sensors* **2022**, *22*, 6231. [[CrossRef](#)]
19. Naboureh, A.; Li, A.; Bian, J.; Lei, G. National Scale Land Cover Classification Using the Semiautomatic High-Quality Reference Sample Generation (HRSG) Method and an Adaptive Supervised Classification Scheme. *IEEE J. Sel. Top. Appl. Earth Obs. Remote Sens.* **2023**, *16*, 1858–1870. [[CrossRef](#)]
20. Kazemi Garajeh, M.; Blaschke, T.; Hossein Haghi, V.; Weng, Q.; Valizadeh Kamran, K.; Li, Z. A comparison between sentinel-2 and landsat 8 OLI satellite images for soil salinity distribution mapping using a deep learning convolutional neural network. *Can. J. Remote Sens.* **2022**, *48*, 452–468. [[CrossRef](#)]
21. Lin, X.; Wu, S.; Chen, B.; Lin, Z.; Yan, Z.; Chen, X.; Yin, G.; You, D.; Wen, J.; Liu, Q. Estimating 10-m land surface albedo from Sentinel-2 satellite observations using a direct estimation approach with Google Earth Engine. *ISPRS J. Photogramm. Remote Sens.* **2022**, *194*, 1–20. [[CrossRef](#)]
22. Naboureh, A.; Bian, J.; Lei, G.; Li, A. A review of land use/land cover change mapping in the China-Central Asia-West Asia economic corridor countries. *Big Earth Data* **2021**, *5*, 237–257. [[CrossRef](#)]
23. Loyola, D.G.; Gimeno García, S.; Lutz, R.; Argyrouli, A.; Romahn, F.; Spurr, R.J.; Pedergnana, M.; Doicu, A.; Molina García, V.; Schüssler, O. The operational cloud retrieval algorithms from TROPOMI on board Sentinel-5 Precursor. *Atmos. Meas. Tech.* **2018**, *11*, 409–427. [[CrossRef](#)]
24. Virghileanu, M.; Săvulescu, I.; Mihai, B.-A.; Nistor, C.; Dobre, R. Nitrogen Dioxide (NO₂) Pollution monitoring with Sentinel-5P satellite imagery over Europe during the coronavirus pandemic outbreak. *Remote Sens.* **2020**, *12*, 3575. [[CrossRef](#)]
25. Shikwambana, L.; Mhangara, P.; Mbatha, N. Trend analysis and first time observations of sulphur dioxide and nitrogen dioxide in South Africa using TROPOMI/Sentinel-5 P data. *Int. J. Appl. Earth Obs. Geoinf.* **2020**, *91*, 102130. [[CrossRef](#)]
26. Kazemi Garajeh, M.; Weng, Q.; Hossein Haghi, V.; Li, Z.; Kazemi Garajeh, A.; Salmani, B. Learning-Based Methods for Detection and Monitoring of Shallow Flood-Affected Areas: Impact of Shallow-Flood Spreading on Vegetation Density. *Can. J. Remote Sens.* **2022**, *48*, 481–503. [[CrossRef](#)]
27. Haque, M.N.; Sharif, M.S.; Rudra, R.R.; Mahi, M.M.; Uddin, M.J.; Abd Ellah, R.G. Analyzing the spatio-temporal directions of air pollutants for the initial wave of COVID-19 epidemic over Bangladesh: Application of satellite imageries and Google Earth Engine. *Remote Sens. Appl. Soc. Environ.* **2022**, *28*, 100862. [[CrossRef](#)]
28. Ghasempour, F.; Sekertekin, A.; Kutoglu, S.H. Google Earth Engine based spatio-temporal analysis of air pollutants before and during the first wave COVID-19 outbreak over Turkey via remote sensing. *J. Clean. Prod.* **2021**, *319*, 128599. [[CrossRef](#)]
29. Prasai, R.; Schwertner, T.W.; Mainali, K.; Mathewson, H.; Kafley, H.; Thapa, S.; Adhikari, D.; Medley, P.; Drake, J. Application of Google earth engine python API and NAIP imagery for land use and land cover classification: A case study in Florida, USA. *Ecol. Inform.* **2021**, *66*, 101474. [[CrossRef](#)]
30. Li, Y.; Fang, H. Real-Time Software for the Efficient Generation of the Clumping Index and Its Application Based on the Google Earth Engine. *Remote Sens.* **2022**, *14*, 3837. [[CrossRef](#)]
31. Titti, G.; Napoli, G.N.; Conoscenti, C.; Lombardo, L. Cloud-based interactive susceptibility modeling of gully erosion in Google Earth Engine. *Int. J. Appl. Earth Obs. Geoinf.* **2022**, *115*, 103089. [[CrossRef](#)]
32. Ghosh, S.; Kumar, D.; Kumari, R. Cloud-based large-scale data retrieval, mapping, and analysis for land monitoring applications with google earth engine (GEE). *Environ. Chall.* **2022**, *9*, 100605. [[CrossRef](#)]
33. Liu, D.; Chen, N.; Zhang, X.; Wang, C.; Du, W. Annual large-scale urban land mapping based on Landsat time series in Google Earth Engine and OpenStreetMap data: A case study in the middle Yangtze River basin. *ISPRS J. Photogramm. Remote Sens.* **2020**, *159*, 337–351. [[CrossRef](#)]
34. Roman-Gonzalez, A.; Navarro-Raymundo, A.F.; Vargas-Cuentas, N.I. Air pollution monitoring in Peru using satellite data during the quarantine due to COVID-19. *IEEE Aerosp. Electron. Syst. Mag.* **2020**, *35*, 73–79. [[CrossRef](#)]
35. Qu, L.A.; Chen, Z.; Li, M.; Zhi, J.; Wang, H. Accuracy improvements to pixel-based and object-based lulc classification with auxiliary datasets from Google Earth engine. *Remote Sens.* **2021**, *13*, 453. [[CrossRef](#)]
36. Velayarce, D.; Bustos, Q.; García, M.P.; Timaná, C.; Carbajal, R.; Salvatierra, N.; Horna, D.; Murray, V. Air quality analysis in lima, peru using the NO₂ levels during the COVID-19 pandemic lockdown. *Atmosphere* **2022**, *13*, 373. [[CrossRef](#)]
37. Shami, S.; Ranjgar, B.; Bian, J.; Khoshlahjeh Azar, M.; Moghimi, A.; Amani, M.; Naboureh, A. Trends of CO and NO₂ Pollutants in Iran during COVID-19 pandemic using Timeseries Sentinel-5 images in Google Earth Engine. *Pollutants* **2022**, *2*, 156–171. [[CrossRef](#)]
38. Abunnasr, Y.; Mhaweji, M. Towards a combined Landsat-8 and Sentinel-2 for 10-m land surface temperature products: The Google Earth Engine monthly Ten-ST-GEE system. *Environ. Model. Softw.* **2022**, *155*, 105456. [[CrossRef](#)]

39. Bera, D.; Chatterjee, N.D.; Ghosh, S.; Dinda, S.; Bera, S. Recent trends of land surface temperature in relation to the influencing factors using Google Earth Engine platform and time series products in megacities of India. *J. Clean. Prod.* **2022**, *379*, 134735. [[CrossRef](#)]
40. Ravindra, K.; Bahadur, S.S.; Katoch, V.; Bhardwaj, S.; Kaur-Sidhu, M.; Gupta, M.; Mor, S. Application of machine learning approaches to predict the impact of ambient air pollution on outpatient visits for acute respiratory infections. *Sci. Total Environ.* **2023**, *858*, 159509. [[CrossRef](#)]
41. Taati, A.; Salehi, M.H.; Mohammadi, J.; Mohajer, R.; Díez, S. Pollution assessment and spatial distribution of trace elements in soils of Arak industrial area, Iran: Implications for human health. *Environ. Res.* **2020**, *187*, 109577. [[CrossRef](#)] [[PubMed](#)]
42. Feizizadeh, B.; Omarzadeh, D.; Kazemi Garajeh, M.; Lakes, T.; Blaschke, T. Machine learning data-driven approaches for land use/cover mapping and trend analysis using Google Earth Engine. *J. Environ. Plan. Manag.* **2023**, *66*, 665–697. [[CrossRef](#)]
43. Li, A.; Song, K.; Chen, S.; Mu, Y.; Xu, Z.; Zeng, Q. Mapping African wetlands for 2020 using multiple spectral, geo-ecological features and Google Earth Engine. *ISPRS J. Photogramm. Remote Sens.* **2022**, *193*, 252–268. [[CrossRef](#)]
44. Alvim, D.S.; Chiquetto, J.B.; D’Amelio, M.T.S.; Khalid, B.; Herdies, D.L.; Pendharkar, J.; Corrêa, S.M.; Figueroa, S.N.; Frassoni, A.; Capistrano, V.B. Evaluating Carbon Monoxide and Aerosol Optical Depth Simulations from CAM-Chem Using Satellite Observations. *Remote Sens.* **2021**, *13*, 2231. [[CrossRef](#)]
45. Ahn, D.H.; Choi, T.; Kim, J.; Park, S.S.; Lee, Y.G.; Kim, S.-J.; Koo, J.-H. Southern Hemisphere mid-and high-latitude AOD, CO, NO₂, and HCHO: Spatiotemporal patterns revealed by satellite observations. *Prog. Earth Planet. Sci.* **2019**, *6*, 1–16. [[CrossRef](#)]
46. Kim, S.; Park, S.-J.; Lee, H.; Ahn, D.H.; Jung, Y.; Choi, T.; Lee, B.Y.; Kim, S.-J.; Koo, J.-H. Evaluation of total ozone column from multiple satellite measurements in the antarctic using the brewer spectrophotometer. *Remote Sens.* **2021**, *13*, 1594. [[CrossRef](#)]
47. Peterson, P.L.; Baker, E.; McGaw, B. *International Encyclopedia of Education*; Elsevier Ltd.: Amsterdam, The Netherlands, 2010.
48. Muñoz, D.F.; Ramírez-López, A. A note on bias and mean squared error in steady-state quantile estimation. *Oper. Res. Lett.* **2015**, *43*, 374–377. [[CrossRef](#)]
49. Willmott, C.J.; Matsuura, K. Advantages of the mean absolute error (MAE) over the root mean square error (RMSE) in assessing average model performance. *Clim. Res.* **2005**, *30*, 79–82. [[CrossRef](#)]
50. Lam, K.F.; Mui, H.; Yuen, H. A note on minimizing absolute percentage error in combined forecasts. *Comput. Oper. Res.* **2001**, *28*, 1141–1147. [[CrossRef](#)]
51. Karimi, B.; Shokrinezhad, B. Spatial variation of ambient PM_{2.5} and PM₁₀ in the industrial city of Arak, Iran: A land-use regression. *Atmos. Pollut. Res.* **2021**, *12*, 101235. [[CrossRef](#)]
52. Phuong, D.T.K.; Nhut, M.C.; Tri, N.D. Air Pollution Assessment Using RS and Gis in Ho Chi Minh City, Viet Nam: A Case Study of Period 2015–2019 for SO₂ and NO₂. In *IOP Conference Series: Earth and Environmental Science*; IOP Publishing: Bristol, UK, 2021; Volume 652, p. 012004.
53. Bugdayci, I.; Ugurlu, O.; Kunt, F. Spatial Analysis of SO₂, PM₁₀, CO, NO₂, and O₃ Pollutants: The Case of Konya Province, Turkey. *Atmosphere* **2023**, *14*, 462. [[CrossRef](#)]

Disclaimer/Publisher’s Note: The statements, opinions and data contained in all publications are solely those of the individual author(s) and contributor(s) and not of MDPI and/or the editor(s). MDPI and/or the editor(s) disclaim responsibility for any injury to people or property resulting from any ideas, methods, instructions or products referred to in the content.